RSC Sustainability

ROYAL SOCIETY OF CHEMISTRY

CRITICAL REVIEW

View Article Online
View Journal | View Issue

Cite this: *RSC Sustainability*, 2025, **3**, 4887

2D transition metal dichalcogenides for photovoltaics, hydrogen production, and CO_2 photoreduction

Kevin Reynold Wijaya,[a] Lina Jaya Diguna, *[b] Annisa Tsalsabila,[cd] Indra Jaya Budiarso, [a] Hermawan Judawisastra,[a] Arramel Arramel, [e] Ferry Anggoro Ardy Nugroho, [fg] Muhammad Danang Birowosuto [h] and Arie Wibowo *[a]

The transition from fossil-based to solar-based energy sources is essential to minimize greenhouse gas emissions. Two-dimensional transition metal dichalcogenides (2D TMDs) have emerged as promising materials for solar energy harvesting due to their tuneable electronic and optoelectronic properties, which can be engineered to enhance their performance in various applications. The utilization of 2D TMDs for solar energy conversion can be achieved through solar photovoltaics, photoelectrochemical (PEC) water splitting for the hydrogen evolution reaction (HER), and carbon dioxide (CO_2) photoreduction. In this review, we provide a comprehensive overview of the fundamental aspects of 2D TMDs, including their structure and electronic and optoelectronic properties, as well as the engineering strategies applied across PV, PEC, and CO_2 photoreduction systems. Variations in 2D TMDs and modification approaches result in distinct multifunctional performances. This outlook highlights the potential for the further exploitation of the unique characteristics of 2D TMDs to achieve high and reliable performances, ultimately accelerating their large-scale commercialization and paving the way for a clean and sustainable future.

Received 27th June 2025
Accepted 11th September 2025

DOI: 10.1039/d5su00494b

rsc.li/rscsus

Sustainability spotlight

The utilization of fossil-based conventional energy remains a major contributor to climate and environmental problems. Solar energy is the most promising renewable energy source, which has not been efficiently utilized yet due to the limited availability of materials that can efficiently harvest the full spectrum of sunlight. Two-dimensional transition metal dichalcogenides (2D TMDs) offer significant potential to address this issue through their tuneable electronic and optoelectronic properties. This review highlights the recent advances in 2D TMDs for solar energy harvesting, aiming to enhance clean energy generation. This work directly aligns with UN SDG 7.2 and 13, which target a substantial increase in the share of renewable energy in the global energy mix and decrease in CO_2 in the atmosphere by 2030, respectively.

[a]*Materials Science and Engineering Research Group, Faculty of Mechanical and Aerospace Engineering, Institut Teknologi Bandung (ITB), Ganesha 10, Bandung 40132, West Java, Indonesia. E-mail: ariewibowo@itb.ac.id*

[b]*Department of Renewable Energy Engineering, Universitas Prasetiya Mulya, Kavling Edutown 1.1, BSD Raya Utama, BSD City, Tangerang 15339, Indonesia. E-mail: lina.diguna@prasetiyamulya.ac.id*

[c]*Department of Physics, Faculty of Mathematics and Natural Sciences, IPB University, Meranti, Bogor 16680, West Java, Indonesia*

[d]*Doctoral Program in Materials Science and Engineering, Faculty of Mechanical and Aerospace Engineering, ITB, Ganesha 10, Bandung 40132, Indonesia*

[e]*Center of Excellence Applied Physics and Chemistry, Nano Center Indonesia, PUSPITEK, South Tangerang, Banten 15314, Indonesia*

[f]*Department of Physics, Faculty of Mathematics and Natural Sciences, Universitas Indonesia, Depok 16424, Indonesia*

[g]*Institute for Advanced Sustainable Materials Research and Technology (INA-SMART), Faculty of Mathematics and Natural Sciences, Universitas Indonesia, Depok 16424, Indonesia*

[h]*Łukasiewicz Research Network—PORT Polish Center for Technology Development, Stabłowicka 147, 54-066 Wrocław, Poland*

1 Introduction

Energy-related problems have raised global concerns driven by the excessive emission of greenhouse gases (GHGs); these are byproducts of energy utilization, which cause a rise in temperature and severe climate disasters. Therefore, transitioning from fossil-fuel energy to cleaner and more renewable energy is an urgent need to respond to global warming and create a sustainable society for the future. Among the various types of renewable energy, solar energy has the highest potency to fulfil the world energy consumption because the Earth receives 4.4×10^{16} W of power from the sun each year.[1] There are several strategies to harvest solar energy such as direct conversion to electricity using photovoltaic (PV) cells,[2] green hydrogen (H_2) production through photoelectrochemical (PEC) water splitting,[3] and hydrocarbon fuel production while reducing the

excess of carbon dioxide (CO_2) in the atmosphere through CO_2 photoreduction.[4] To achieve efficient sunlight conversion into electricity, hydrogen, or hydrocarbon fuels from CO_2, the development of advanced photocatalyst materials is inevitable and plays a crucial role.

In this context, two-dimensional (2D) materials have attracted much attention because they can maximize light absorption even with a low flux density and shorten the electron pathways to reach the active sites due to their large surface area.[5,6] 2D materials such as graphene, transition metal dichalcogenides (TMDs), and graphitic carbon nitride (g-C_3N_4) have been employed to achieve solar light to electricity conversion,[7–9] green H_2 production,[10–12] and CO_2 removal.[13–15] Among them, 2D TMDs, which are composed of a plane of transition metal atoms sandwiched between two planes of chalcogenide atoms, offer significant potential to address this issue through their tuneable electronic and optoelectronic properties.[11,16] 2D TMDs experience a transition from indirect to direct bandgap when their size is reduced to 2D from their bulk counterparts, which prolongs the recombination time of excited electrons and holes, thus enhancing the photocatalytic activity.[16] 2D TMDs also possess strong electron–photon interactions since 2D TMDs' monolayer can absorb up to 20% of light in the spectral region.[17] Their bandgap can be tuned by changing the type of transition and chalcogenide atoms, which render them with exceptional flexibility. 2D TMDs also have high strain tolerance, which makes them interesting for application in flexible solar cells.[18,19] Furthermore, the presence of dangling-bond-free surface in layered 2D TMDs enable the fabrication of in-plane and out-of-plane heterostructures.[20]

To see the bigger picture, Fig. 1 shows the increasing research trend in TMD-based materials, especially PV, light-driven hydrogen evolution reaction (HER) catalysts, and CO_2 photoreduction from 1977 (the year TMDs were first reported) to 2025. Additionally, the data were collected from Scopus publications using three keywords, *i.e.*, 'TMDs for solar cell or photovoltaic applications', 'TMDs for photocatalytic hydrogen evolution reaction', and 'TMDs for photocatalytic CO_2 photoreduction'. Historically, the initial report on this system was written in 1977. Then, Tributsch used MoS_2 to substitute CdS or GaAs in solar cell applications. He found that the use of MoS_2 enabled resistance to rapid anodic PEC disintegration.[21] In 1988, WS_2 was found to facilitate photocatalytic HER as a co-catalyst, marking a new milestone in TMD-based materials for photocatalytic application.[22] Further research in 2008 finally discovered that MoS_2, which was firstly use for solar cell applications, also performs extremely well as a co-catalyst for HER.[23] Inspired by the discovery of graphene in 2004 and the fact that TMDs have a layered structure, Mak *et al.* demonstrated the feasibility of making atomically thin MoS_2 and observed the evolution of the optical and electronic properties of MoS_2 as a function of layer number in 2010.[24] They found that upon thinning, MoS_2 shifts from an indirect to direct bandgap semiconductor and exhibits 10^4 stronger luminescence properties compared to its bulk counterpart. Upon continuing development, researchers finally fabricated a TMD-based photocathode using WSe_2 for HER application in 2013. In 2014 and following the rapid development of 2D TMDs, it was discovered that van der Waals (vdW) heterostructures between MoS_2/WS_2 exhibit ultrafast hole transfer (~50 fs) favorable for efficient charge separation.[25] This marks the potential of TMDs as superior materials in optoelectronic devices and light harvesting applications. The development of TMDs did not stop there, where the development of these materials continued in 2017 when it was discovered that WSe_2 has the ability to drive

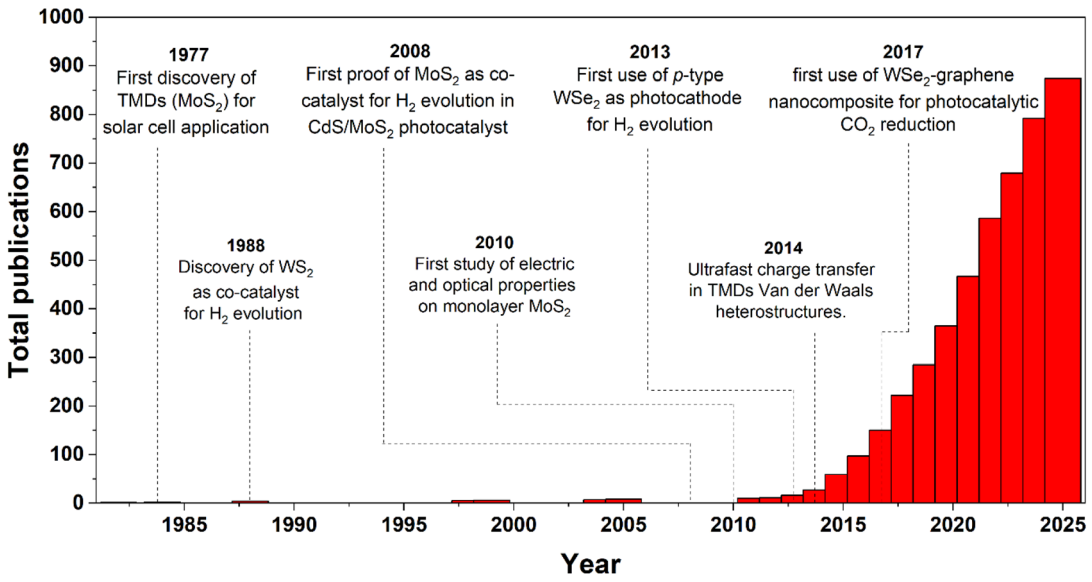

Fig. 1 Research trend on TMDs for solar cell application, H_2 production, and CO_2 photoreduction. These data were collected from Scopus publications using three keywords: 'TMDs for solar cell or photovoltaic applications', 'TMDs for photocatalytic hydrogen evolution reaction', and 'TMDs for photocatalytic CO_2 photoreduction'. The search was restricted to publications from 1977 (the year TMDs were first reported) to 2025.

photocatalytic CO_2 reduction, opening a new window for TMD materials in photocatalytic applications.[26]

Nowadays, 2D TMDs have undergone extensive development and modifications to enhance their properties and performance, making them well-suited for various emerging applications. Although numerous reviews have explored the individual roles of 2D TMDs in solar energy applications[8,27–29] and their modification strategies,[30,31] an integrated perspective that connects their fundamental properties with performance across PV, H_2 production through PEC cells, and CO_2 photoreduction remains lacking. This review aims to fill that gap by systematically examining the structure–property relationships of 2D TMDs and highlighting how different engineering strategies influence their multifunctional performance. By bridging the insights from diverse applications, this work offers a comprehensive framework that not only summarizes recent progress but also identifies key challenges and future research directions. Therefore, this review provides both a timely update and a novel contribution to the body of knowledge, supporting the rational design of 2D TMD-based systems for next-generation solar energy harvesting technologies. The summary in this review can serve as a foundation for future research, particularly in guiding material design for advanced applications. Furthermore, different modifications of 2D TMDs may be tailored to suit specific applications. Therefore, this review can be utilized for materials selection to further commercialize the advanced application of 2D TMDs.

2 Fundamentals of 2D TMDs

2D TMDs have superior properties for renewable energy applications such as tuneable bandgap and wide range light absorption, and their properties are also correlated with their structure and modification. Therefore, understanding the fundamental structure, properties, and modification of 2D TMDs has become crucial to tune and find suitable materials and performances for specific solar energy harvesting applications. For example, the electronic and optoelectronic properties of 2D TMDs have been widely studied and discussed in relation to their applications in solar energy. These properties are closely related to their electron movement, crystal structure, and band structure, which can be induced by tuning their layer thickness and other engineering.[11,16,32] The following section will provide an in-depth explanation of the fundamental aspects and the modifications of these properties and their performance including their crystal structures and phases.

2.1 Crystal structure

The crystal structure of 2D TMDs is determined by the stacking arrangement of transition metal and chalcogenide atoms, which form a monolayer. 2D TMD monolayers are composed of a trilayer sandwich structure, X–M–X, which is a covalently bonded unit, where X and M are chalcogen and transition metal atoms, respectively.[33] Typically, 2D TMD monolayers can be classified as two phase, hexagonal symmetry (1H) and octahedral (1T) phase. The difference lies in one of the dichalcogenide layers, which is rotated 180° relative to the other dichalcogenide layer within the same structure, as illustrated in Fig. 2a.[34] The 1H phase has an ABA stacking sequence, while the 1T phase has an ABC stacking sequence because of its horizontally shifted one chalcogen layers (Fig. 2a).[33,35] In the 2D layered structure of TMDs, the structures are built from hexagonally packed planes stacking on top of each other.[16,36] Their inter-monolayers are bonded *via* vdW bonding, while the atoms in the same layer are bonded by strong covalent bonding.[16,37,38] It is an advantage to modify 2D TMDs to gain heterostructure materials. The structure of layered 2D TMDs is polymorph depending on the different ways of stacking and can be categorized as 1T, hexagonal trigonal prismatic (2H), rhombohedral (3R).[16,31,33,39,40] The most common structures of 2D TMDs are 2H and 1T.[31,40] The 2H phase is stable in nature and room temperature, except for WTe_2, whereas 1T is a metastable phase and coexisting phases (distorted phase) such as 1T′, 1T″, and 1T‴ (Fig. 2b), and the other phases can be considered unstable phases at room temperature.[31,36,41,42] The shift in phase from 1T to 1T′, 1T″, and 1T‴ phase is a lattice distortion phenomenon, which induces band inversion.[35,43]

Alkali metal intercalation and water exfoliation are commonly used to produce 2D TMDs from their bulk forms.[40,42] Alkali intercalation can be synthesized through electrochemical intercalation (Fig. 3a),[44] water exfoliation (Fig. 3b),[45] and also chemical intercalation.[46] Similar to other 2D TMDs, the synthesis route by alkali metals (usually lithium) intercalation and exfoliation can produce the 1T phase from 2H-phase 2D TMDs.[39,47] Another way to synthesize 1T-phase 2D TMDs involves immersing 2H phase 2D TMDs into a solution of butyllithium (*n*-BuLi).[48] Reversibly, the 1T phase can be transformed back to the 2H phase by annealing at around 70 °C.[39,48] Also, the impurities in 2H phase 2D TMDs such as Re or Nb will transform the 2H phase to 3R phase.[36] Another study showed

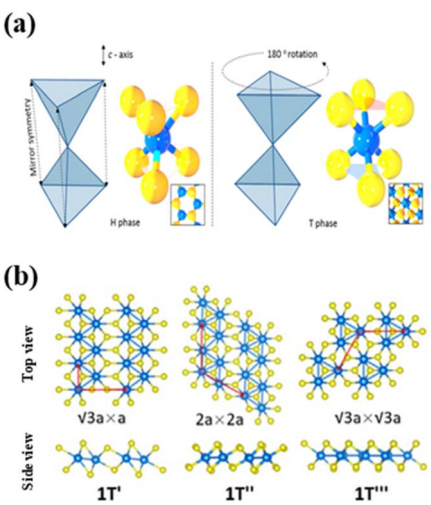

Fig. 2 (a) Structure of H phase (left) and T phase (right) in typical TMDs. Reproduced from ref. 34 with permission from the American Chemical Society, copyright 2018. (b) Crystal structure of TMDs' distorted phases (1T′, 1T″, and 1T‴). Reproduced from ref. 41 with permission from Wiley-VCH Verlag GmbH & Co., copyright 2011.

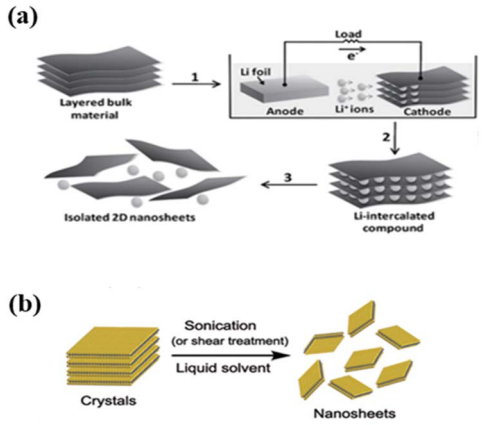

Fig. 3 Methods to generate 2D TMDs from their bulk counterparts: (a) electrochemical intercalation. Reproduced from ref. 44 with permission from Wiley-VCH Verlag GmbH & Co., copyright 2011; (b) water exfoliation. Reproduced from ref. 45 with permission from Wiley-VCH Verlag GmbH & Co., copyright 2016.

that Re-doped $MoSe_2$ can provide phase transitions from the 2H phase to either the 1T or 1T′ phase.[49] The concentration of doping and parent phase plays a crucial role in determining the result of the phase transition. Each phase of 2D TMDs has different properties that can utilized for different applications. In photocatalysts, structural differences lead to variations in their catalytic activity. For example, the 3R phase has the highest catalytic activation, followed by the 1T and 2H phases.[50,51] Therefore, the synthesis method and selection of 2D TMD structure and phase are important to gain targeted and specific properties and performances related to the application.

2.2 Electronic properties

The tuneable layer thickness and band gap of 2D TMDs are the big advantages for a broad range of applications in electronic and optical properties. Reducing the layer thickness of TMDs from bulk to 2D results in the evolution of their band structure and induces quantum confinement.[5,52] The indirect band gap of TMDs turns into a direct band gap in 2D TMDs, which show an increasing band gap compared to their bulk counterparts.[31,40] As seen in Fig. 4a, the valence band (VB) reaches the maximum, and the conduction band (CB) becomes the minimum.[53] The band gap of 2D TMDs cover the entire visible and infrared (IR) range (1.1–2.1 eV).[40] For example, bulk 2H–MoS_2 has an indirect band gap of 0.88 eV, but turns to a direct band gap in monolayer form ref. 31. Using density functional theory (DFT), Zhang *et al.* successfully examined the thermodynamically stable phase, and the band alignment corresponds to the VB maximum and CB minimum in several 2D TMD vdW heterostructures.[54] A reduction in the number of MoS_2 or other 2D TMD layers leads to relatively stable direct excitonic states near the *K* point, whereas those at the *Γ* point exhibit a significant shift from indirect-to-direct transition.[31,55,56] The broken inversion symmetry causes the CB minima at the K and K′ points in the Brillouin zone to degenerate, while being inequivalent at the same time, giving rise to the valley degree of freedom for

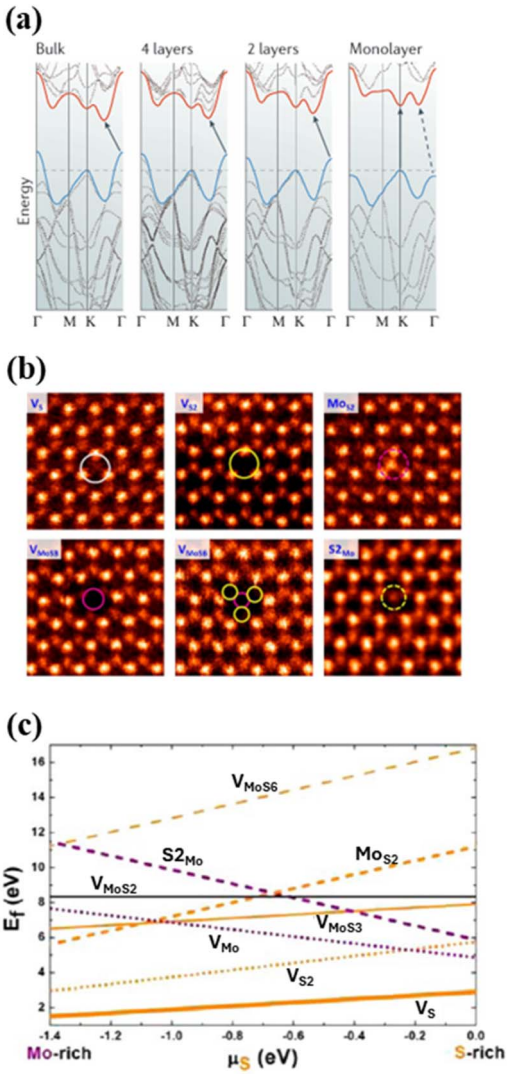

Fig. 4 (a) Indirect-to-direct band gap transition as a result of reducing TMD layers. Reproduced from ref. 53 with permission from Macmillan Publisher, copyright 2014. Intrinsic chalcogen defects in monolayer MoS_2: (b) atomic resolution images and (c) formation energies of different point defects as a function of the chemical potential of sulfur. Reproduced from ref. 62 with permission from the American Chemical Society, copyright 2013.

electrons and holes.[56] A study showed that the interlayer coupling between two vdW heterostructure-stacked 2D layers can be adjusted to give novel properties, whether arranged in a homostructure or heterostructure.[57] It is also known that external factors such as strain can tune the electronic band structure.[17,58–60] For example, the bandgap of MoS_2 can be tuned to 100 meV per 1% strain.[55] As the imposed strain increases, both the direct and indirect bandgaps decrease, with the indirect bandgap reducing at a faster rate. This leads to lower emission efficiency in highly strained monolayers.[61]

Heteroatom doping by incorporating metal or non-metal atoms in the structure of 2D TMDs resulted in the modification of their corresponding electronic structure. In general, heteroatom doping of 2D TMDs could modify their d-band

structure and reduce the Gibbs free energy change, thereby stabilizing and optimizing the material structure. Metal doping contributes to the stabilization and optimization of the Gibbs free energy changes. Beyond metal doping, non-metal doping induces structural distortion in the crystal lattice. This geometric modification could induce the desired phase transition. Recent engineering effort by electron doping was proposed to form a 1T MoS_2/single-walled carbon nanotube (SWNT) heterostructure.[63] Nayak *et al.* observed an increase in the band gap of tungsten-doped (in range of 0.00–1.00 weight composition) MoS_2 monolayers from ~1.735 eV to ~1.875 eV.[64]

It is generally understood that different electronic bands and crystal structures promote different charge carrier mobility. Among the 2D TMD structures, 1T and its distortion phases as a metallic phase have higher electronic conductivity and active site density compared to the other phases.[63] Simply, electronic conductivity can be enhanced by inducing a semiconductor-to-metal transition that results in a reduction in bandgap energy and increase non-bonding electron. The transition can be induced by engineering chalcogen atom defects, which can be achieved in various ways such as chemical vapour deposition. Chalcogen defects (Fig. 4b) lead to a change in the Fermi level (Fig. 4c), which induces a semiconductor-to-metal transition.[62] Fig. 4b and c showed six cases of chalcogen defects including V_S (monosulfur vacancy), V_{S2} (disulfur vacancy), Mo_{S_2} (antisite defects, where an Mo atom substitutes an S_2 column), V_{MoS_3} (vacancy complex of Mo and nearby three sulfur), V_{MoS_6} (vacancy complex of Mo nearby three disulfur pairs), and S_{2Mo} (S_2 column substituting an Mo atom).[62] Atomic vacancies form an n-type conduction in general 2D TMDs, whereas oxygen substitution in $PdSe_2$ FET fabrication forms p-type conduction.[32]

Theoretical calculation predicts that 2D TMDs have electron mobility in the range of 10–1000 $cm^2\ V^{-1}\ s^{-1}$ at room temperature.[65] Naturally, 2D TMDs show experimentally low mobility due to the collective effect caused by foreign impurities, and extrinsic factors become a limitation for 2D TMDs. This is indicated by their lower experimental values than theoretical values. The theoretical phonon-limited mobility of monolayer MoS_2 and WS_2 at room temperature is ≈ 410 $cm^2\ V^{-1}\ s^{-1}$ and ≈1100 $cm^2\ V^{-1}\ s^{-1}$, whereas the experimental record is only 150 $cm^2\ V^{-1}\ s^{-1}$ and 80 $cm^2\ V^{-1}\ s^{-1}$, respectively.[65] Besides foreign impurities and extrinsic factors, the morphology and crystal structure of 2D TMDs are also known as factors that influence their mobility carrier and conductivity. In the case of MoS_2, the 1T phase is 10^7 times more conductive and has enhanced energy density than the 2H phase.[40,61,65] Also, ZnO/WSe_2 with type-II vdW heterojunctions was successfully fabricated by Hu *et al.* and exhibited a small carrier effective mass, which is proportional with higher carrier mobility, with the minimum and maximum mobility of 381.20–1263.74 $cm^2\ V^{-1}\ s^{-1}$, respectively.[66]

The electronic properties of 2D TMDs are highly tuneable by reducing their layer thickness, strain, doping, phase transition, and defect engineering. These unique features enable direct modulation of their indirect-to-direct band structure, carrier mobility, and conductivity, thereby offering versatile control over their electronic responses. The flexibility of their band structure and carrier mobility highlights the potential of 2D TMDs for advanced electronic applications.

2.3 Optoelectronic properties

It is widely accepted that 2D TMDs show strong light–matter interaction, light absorption, and large excitonic binding energy. Their unique and remarkable optical and optoelectronic properties are attributed to the quantum confinement effects induced by the transition of their electronic band structure from an indirect to direct bandgap. An indirect band gap has a less efficient photon absorption/emission mechanism.[67] This implies a decline in the optoelectronic performance of 2D TMDs. The interlayer interactions between transition metal ions and chalcogenide ions consist of Coulomb interactions. Increasing the Coulomb interactions and effective masses of electrons and holes has a big impact on electron–hole pair recombination.[55] Optoelectronic properties are two important properties that are normally considered.

The optical transition can be either a direct or indirect transition. A direct transition requires only a photon for electron excitation, whereas an indirect transition also requires another phonon (lattice vibration). The light absorption by 2D TMDs is influenced by their low bandgap energy. The optical absorption by 2D TMDs can reach 10% at bandgap resonances because of the domination of excitonic transitions.[55] For example, single-layer MoS_2 can absorbs >10% of incident light at wavelengths of 615 and 660 nm, and can be even higher at a lower wavelength.[16] Increasing the bandgap of 2D TMDs compared to their bulk counterparts can result in an enhanced performance given that 2D TMDs can exhibit 10^4 times stronger luminescence than their bulk counterparts. This phenomenon is induced by the quantum confinement effect. High binding energy and strong photoluminescence (PL) are two aspects that are highly considered for the application of 2D TMDs in optoelectronic devices such as solar cells. It was reported that the presence of electroluminescence (EL) in monolayer MoS_2 was limited at the metal contacts and resulted in a low quantum efficiency (10^{-5} for monolayer MoS_2).[57] In terms of photocatalysts, 2D TMDs are promising materials because of their sheet-like layered structure, high surface area, and excellent light absorption.

Further, the optical and optoelectronics properties of 2D TMDs can be enhanced by applying defect engineering. Among the various types of defect engineering that can be applied, atomic interstitials have a strong effect on the optical and optoelectronics properties. Oxygen atomic interstitials influence localized excitons in terms of length scale, causing photons to be emitted one at a time.[32] Introducing chalcogen atom defects in the outmost layer of 2D TMDs can enhance their optoelectronic performance.[32] Also, chalcogen atom defects have an impact on the long-lived excitonic transition with a stable valley pseudospin.[32]

In the light-2D TMD interaction, photoexcited electron–hole pairs will be separated by the built-in electric field, resulting in a photocurrent. N-type MoS_2 and WSe_2 show poor external quantum efficiencies (EQEs) with a value of 12% for WSe_2/

MoS_2.[57] Alternatively, Wang *et al.* showed that p-GaTe/n-MoS_2 has a high EQE (61.68%).[68] This significant difference is attributed to its ultrathin junction, which enables efficient and rapid charge transfer due to the presence of a depletion region and the suppression of excitons (or minority carriers). The formed heterojunction will reinforce and increase the light absorption range, also resulting in a red shift in light absorption.[69] Furthermore, the generation, separation, and transport processes of photoexcited electron–hole pairs can be enhanced by applying a back-gate voltage.[57] Another study showed that different stacking orientations can exhibit different optoelectronic properties. Vertically composition-controlled (VCC) layered $Mo_{1-x}W_xS_2$ has been successfully synthesised *via* the sulphurization of $Mo_{1-x}W_xO_y$. VCC layered $Mo_{1-x}W_xS_2$ has strong interlayer coupling and broadband light absorption. Research shows that VCC layered $Mo_{1-x}W_xS_2$ exhibits a photocurrent in the range of 1.2–2.5 eV, which is larger than that of multilayer WS_2 (1.3–2.1 eV) and multilayer MoS_2 (1.2–1.8 eV).[70] In another experiment by Gong *et al.*, they synthesized a WS_2/MoS_2 vertical heterostructure. In the monolayer MoS_2 and bilayer WS_2/MoS_2 region, the PL spectrum shows a single strong peak at 680 nm (1.82 eV) and three peaks at 630 nm (1.97 eV), 680 nm (1.82 eV), and 875 nm (1.42 eV).[71] The first two peaks in the bilayer region come from the direct excitonic transition of the WS_2 and MoS_2 monolayers, respectively. The new strong peak at 875 nm suggests a direct excitonic transition in the bilayer heterostructure that has not been observed before. Thus, the coupling between the WS_2 and MoS_2 layers exhibits a direct bandgap at a lower energy. Therefore, they are expected to absorb in a wide range of the solar spectrum.

The remarkable optoelectronic properties of 2D TMDs are governed by their tuneable band structures, strong excitonic effects, and efficient light–matter interactions. Therefore, these unique features make 2D TMDs promising materials for advanced optoelectronic applications with further performance improvements through advanced engineering.

3 Application of 2D TMDs as solar energy harvesters

3.1 Photovoltaic application

2D TMDs have become more attractive for solar energy conversion due to their excellent optical absorption, tuneable band gaps, high carrier mobility, and self-passivated surfaces, wherein nowadays, 2D TMD materials have expanded at a very high pace, relying on their ultimate atomic thicknesses.[72–74] The ability of 2D TMD monolayers (MoS_2, $MoSe_2$, and WS_2) to absorb up to 5–10% incident sunlight at a thickness of less than 1 nm potentially allows the fabrication of ultrathin PV devices.[72] The investigation of 2D monolayers from group 4 to 11 2H–TMDs showed that the presence of excitons affects the band alignment and the power conversion efficiency (PCE), in which the PCE of $MoSe_2$/WS_2 heterojunction is calculated to be improved ~3.65% by exciton effects.[75] Additionally, 2D a CH_3-NH_3PbI_3/HfS_2 vdW heterostructure was modelled and proposed to be an efficient light-absorbing material for PV application.[76] Meanwhile, mechanical distortion-induced bulk photovoltaic behavior has been reported in 2D $MoTe_2$ due to its phase transition and broken inversion symmetry, featuring photocurrent responses caused by in-plane polarity.[77]

An examination of the efficiency limits of multilayer 2D TMD solar cells has demonstrated that single-junction solar cells with 2D TMD films as thin as 50 nm could in practice achieve a PCE up to 25%.[78] Similar to other optoelectronic devices, 2D TMDs could be assembled in stacked and lateral architectures in vdW heterojunction solar cells.[79] In a vertical structure, a 2D WSe_2/MoS_2 p–n heterojunction with a thickness of ~10 nm and indium tin oxide (ITO) electrode was suggested as a transparent solar cell with visible light transparency of ~80%, and with further fluoropolymer (Teflon AF2400) passivation, the PCE could be improved from 7.99% to 10% under halogen lamp illumination of 1.91 mW cm^{-2}.[80] In another study on vertical WSe_2/MoS_2 p–n heterojunction devices, atomically thin WO_x as a hole transport layer (HTL) has been reported to form a low Schottky barrier and favorable interface band alignment, thus significantly increasing the PCE from 0.7% to 5.0%.[81] Considering the excellent properties of 2D TMDs for flexible high specific-power PVs, flexible solar cells using ~200-nm-thick WSe_2 absorbers have been successfully fabricated on lightweight flexible polyimide substrates with a PCE of 5.1% and specific power of 4.4 W g^{-1}, and demonstrated the same *J–V* characteristics in flat and bent states with the substrate bending radius of 4 mm under AM 1.5G illumination.[82] Moreover, a WSe_2 PV device with a high PCE of 5.44% has been successfully achieved through contact engineering, as shown in Fig. 5a and b, which is a combined effect of an enhanced internal electric field and electron selectivity owing to the WO_x layer at the top contact region and improved photon recycling and carrier extraction due to the effective bottom contact scheme.[83] Conversely, for the lateral structure, 2D monolayer WSe_2–MoS_2 p–n heterojunction solar cells have also been explored with the PCE of 2.56% achieved under AM 1.5G illumination, revealing the prospect of atomically sharp lateral p–n interface as next-generation PVs.[84] Recently, 2D MoS_2 diodes with geometrically asymmetric contact areas (AS-MoS_2) have demonstrated a high current rectification ratio of $\approx 10^5$, facilitating efficient PV charge collection, while the corresponding lateral 2D solar cell achieved a PCE of 3.16% under one sun illumination, as shown in Fig. 5c.[27] Further transferring the AS-MoS_2 device onto a flexible polyethylene terephthalate (PET) substrate has shown high photocurrent and PCE retentions of 94.4% and 88.2% after 5000 bending cycles at a bending radius of 1.5 cm, respectively, as depicted in Fig. 5d.[27] These advancements in 2D TMD-based flexible and lightweight PVs pave the way for practical applications beyond the current use of traditional silicon solar cells, such as portable and wearable self-powered electronic devices.

The unique properties of 2D TMDs feasibly match the requirements for various building blocks especially for third-generation PVs to deliver outstanding performances and turn out to be attractive alternatives to conventional solar cells. In the case of emerging PV technologies, different utilization approaches of 2D TMDs have been conducted not only in the light-absorbing layers but also in other building blocks such as

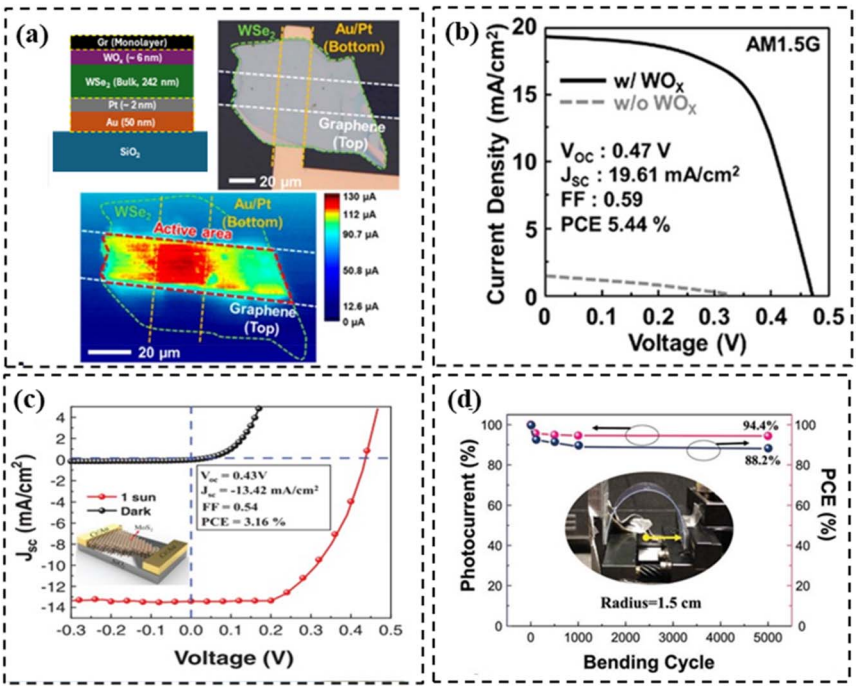

Fig. 5 (a) Schematic structure of a WSe_2 photovoltaic device (top left), top-view optical microscopy images of the device (top right) and corresponding spatial photocurrent map with the active area (bottom) and (b) photovoltaic effect of the devices under 1 sun AM 1.5G illumination. Reproduced from ref. 83 with permission from the American Chemical Society, copyright 2022. Solar cell based on 2D MoS_2 with geometrically asymmetric contact areas (AS-MoS_2): (c) *J*–*V* characteristics under 1 sun illumination (inset: schematic of the AS-MoS_2 solar cell with two Cr/Au electrodes) and (d) photocurrent and PCE retention after up to 5000 bending cycles at a bending radius of 1.5 cm (inset: image of AS-MoS_2 solar cell on PET under bending test). Reproduced from ref. 27 with permission from Wiley-VCH Verlag GmbH & Co., copyright 2023.

the charge carrier transport layers and counter electrodes, along with their multiple integration to fabricate solar cells. In perovskite solar cells (PSCs), a parallel tandem structure consisting of two absorbing layers of $CH_3NH_3PbI_3$ and $MoTe_2$ with cascaded bandgaps has been proposed to broaden the light absorption to the near-infrared solar spectrum.[85] Besides, the incorporation of 2H phase $MoSe_2$ nanosheets in a perovskite film improved the PCE to 22.80% compared to that of 20.92% for the control device and maintained 80% of its initial efficiency under 15–20% RH at room temperature for 1000 hours in air.[86] In solar cell applications, the energy offset at the functioning layer interfaces should enable the efficient separation of photoexcited electron and hole pairs, and drive them to move in opposite directions. In p–i–n PSCs, 2D TMDs have been shown as potential HTLs, where replacing the acidic and hygroscopic-natured PEDOT:PSS with 1T-rich 2D MoS_2 and WS_2 prepared by lithium intercalation reaction leads to an increase in PCE from 12.44% to 14.35% and 15.00%, respectively.[87] Predominately, the metallic 1T phase of 2D TMDs possesses higher conductivity than that of their semiconducting 2H phase.[88,89] Furthermore, 2D MoS_2 nanoflakes have been introduced as a buffer layer between the perovskite layer and HTL, resulting in improved stability of organometallic-halide PSCs with 93.1% of their initial PCE maintained after 1 h under continuous sun illumination due to their role as both a protective layer and additional HTL.[90] The application of 2D MoS_2 as a buffer layer for the HTL, along with graphene as the electron transport layer (ETL) has been extended to large-area perovskite solar modules, achieving PCEs of 13.4% and 15.3% on the active areas of 108 cm^2 and 82 cm^2, respectively.[91] The synergic use of 2D materials as intra and inter layers in halide PSCs by combining graphene into ETL, MXenes into perovskite, and f-MoS_2 at the perovskite/HTL interface has resulted in the PCEs of 17.2% and 14.7% for the large-area modules of 121 cm^2 and 210 cm^2, respectively.[92] The employment of 2D material-based surface engineering in perovskite solar panels has been accomplished, in which nine panels were successfully integrated with a total panel area of 4.5 m^2 in a stand-alone solar farm infrastructure with the nominal power (P_n) exceeding 250 W and an almost monotonic reduction in the solar farm P_n during nine months of operation.[93] Furthermore, as a buffer layer to ETL, an atom-thick 2D TiS_2 layer grown on the surface of (001)-faceted and single-crystalline TiO_2 nanograss has been reported to decrease the trap density in PSCs, and then enhance their PCE from 18.14% to 18.73%.[94] The simultaneous application of both MoS_2 and WSe_2 in the hole and electron transport sides of PSCs, respectively, has been reported to improve not only their efficiency from 18.22% to 19.24% but also their performance stability over 1000 h under damp heat (85 °C and 85% relative humidity) conditions.[95] Here, 2D TMD interlayers facilitate efficient charge transfer along with passivation and strain-release effects to enable the device stability. The potential use of 2D TMDs as charge transporting layers has also been investigated for the application of organic solar cells (OSCs).[96,97] The employment of 2D

$MoSe_2$ quantum dots (QDs) as a subphoto sensitizer and pinhole-free HTL resulted in a PCE of 18.29% for PM6:L8-BO-based OSCs, which is comparable to that of 18.22% for the control device with a PEDOT:PSS HTL.[96] Furthermore, the use of ZnO modified by 2D $ZrSe_2$ as a composite ETL in OSCs with PM6:L8-BO as an active layer could achieve a PCE of 18.24%, which is higher than that of the pure ZnO ETL device of 17.34%, as shown in Fig. 6a.[97]

The high conductivity of 2D TMDs has driven their exploitation as counter electrodes, particularly as substitutes for the expensive and scarce Pt electrodes commonly used in dye-sensitized solar cells (DSSCs). Few-layer $MoSe_2$ on an Mo film has been shown to have high catalytic activity towards iodide/tri-iodide redox shuttles and yield a PCE of 9.00%, which is higher than that generated from an identical photoanode coupled with Pt on fluorine-doped tin oxide (FTO) of 8.68%, in which the obtained PCE values clearly correspond to the measured sheet resistances of $MoSe_2$/Mo and Pt/FTO of 0.29 and 12.60 Ω sq^{-1}, respectively.[99] The design of heterostructures has been attempted by fabricating vdW interacted WSe_2/MoS_2 heterostructures on FTO substrates *via* physicochemical routes, and their employment as counter electrodes for DSSCs resulted in a PCE of 8.44%, which is comparable to that using Pt of 8.73%, owing to the generated interfacial conduction and active facet sharing, thereby improving the catalytic activity of tri-iodide reduction.[100] Furthermore, a hybrid bilayer of MoS_2/$MoTe_2$ on FTO has also been used as a counter electrode in DSSCs with the resulting PCE of 8.07%, which was higher than that of pristine MoS_2 (6%) and $MoTe_2$ (7.25%) and comparable to that with a Pt counter electrode (8.33%), suggesting the synergistic properties between MoS_2 and the metallic phase of $MoTe_2$.[101] Additionally, the counter electrode engineering of a 2D $MoSe_2/WS_2$ heterostructure achieved a PCE of 9.92% with a photocurrent density of 23.10 mA cm^{-2} due to the efficient interfacial transport and active facet edges, thus enriching the electrocatalytic activity.[102] Alternatively, a hybrid composite material cathode of $WS_2/MoCuO_3$ supported with 0.9 wt% graphene QDs (0.9 wt% WM@GQDs) exhibited a PCE of 10.38%, which is higher than that of the Pt electrode of 10.26%, and electrochemical impedance spectroscopy (EIS) measurements confirmed its lower charge transfer resistance, as shown in Fig. 6b.[98]

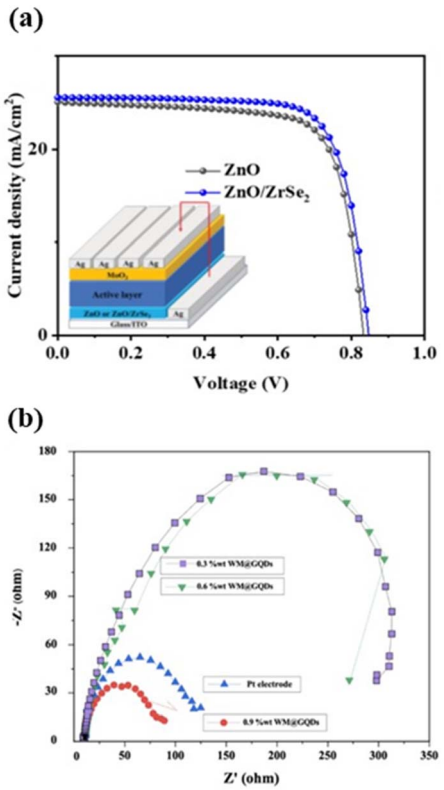

Fig. 6 (a) *J*–*V* curves of OSCs with PM6:L8-BO as the active layer and different ETLs measured at AM 1.5G irradiation (inset: schematic of the OSC). Reproduced from ref. 97 with permission from Wiley-VCH Verlag GmbH & Co., copyright 2024. (b) Electrochemical impedance spectroscopy profiles of different counter electrodes for DSSCs. Reproduced from ref. 98 with permission from Springer Nature, copyright 2023.

Material engineering and device architectures should be further developed to optimize the PV performances and stability. In this regard, the data-driven approaches of artificial intelligent and machine learning model hold significant potential to accelerate promising material discovery and design.[103,104] The integration of 2D TMDs into large-area solar panels was attempted, which may optimize their utilization in real PV applications.[93] Therefore, further investigation to bring the use of 2D TMDs to the next level should be carried out carefully. Here, all the achieved high performances of 2D TMD-based PV should be also coupled with reliable and safe packaging technology, and then subjected to accelerated life testing under sequential and combined-environmental stress factors such as humidity, temperature, thermal cycles, and mechanical loads. The large-area, uniform, and high-quality growth of 2D TMD layers should be pursued especially with the development of roll-to-roll deposition.[105]

3.2 Hydrogen production from PEC cells

H_2 is considered future clean energy due to its high-density energy (120.94 MJ kg^{-1}),[106] environmentally friendly production, and no production of toxic gas when combusted. H_2 serves as a product of clean energy conversion from solar energy into chemical energy, which can be stored.[107] One of the sustainable and environmentally friendly routes to produce H_2 energy is through PEC water splitting utilizing solar light.

PEC cells consist of at least a single photoelectrode either as the photoanode or photocathode and electrolyte. In the case of a single photoelectrode, external bias is needed to guide the accumulation of electrons and holes at the cathode and anode, respectively. One advantage of using PEC for H_2 generation is the lower required external bias compared to conventional electrochemical devices for water splitting. In theory, 1.23 V is needed to drive the water splitting reaction, while practically it ranges from 1.5–2.0 V. Using PEC, this potential can be lowered because semiconductors can produce electrons from solar irradiation. Furthermore, PEC can be extended to a dual

photoelectrode system, where a bias-free device might be realized to drive the water splitting reaction. Typical dual photoelectrode systems use p-type and n-type semiconductors as the photocathode and photoanode, respectively. In PEC, either one or two photoelectrode configurations, an external circuit is placed to transfer separated charge carriers to the other photoelectrode to participate in the HER or oxygen evolution reaction (OER).

Importantly, each CB maximum and VB minimum of the photoelectrode must be more negative and positive than the reduction and oxidation potential of water, respectively (Fig. 7).[108,109] Materials that are favourable to achieve OER are HfS_2, $HfSe_2$, ZrS_2, and $ZrSe_2$. Conversely, the materials that are favourable for HER are $MoTe_2$, $PtTe_2$, WTe_2, and WSe_2. Interestingly, almost all transition metal disulfides such as MoS_2, $MoSe_2$, PtS_2, WS_2, and ReS_2 are favourable for both HER and OER except for Hf and Zr metal. Additionally, this implies that PEC cells using both a photoanode and photocathode are necessary to provide more efficient cells, while utilizing layered 2D TMDs that have a relatively narrow band gap to enable the absorption of sunlight in a wide range. In PEC cells, 2D TMDs can be applied as photoelectrodes, photocatalysts, or co-catalysts. The following sections will discuss the application of 2D TMDs in each of these components of PEC cells.

3.2.1 2D TMDs as photoelectrode. A crucial factor is that the performance of PEC cells heavily depends on their photoelectrode. The photoelectrode is usually made by depositing a photocatalyst onto a conductive substrate such as ITO, FTO, graphite, and metal. The photoelectrode must have a strong bond between the substrate and photocatalyst, ability to absorb a wide light spectrum, shorten the charge pathway, and facilitate the water splitting reaction. The strict requirements of photoelectrodes demand sophisticated materials to be used as the photocatalyst.

2D TMDs are considered promising materials as photoelectrodes because of their ability to absorb a broad light wavelength through their tuneable bandgap. The wider the wavelength range of solar-light that can be utilized, the more efficient the photoelectrode is to produce hydrogen.[110] The 1T phase of 2D TMDs can be utilized as an electron acceptor and suppress the charge recombination process, while the 2H phase can absorb light to generate excitons.[29] A study reported that 2D TMDs as photoelectrodes have a lower efficiency than the Si electrode that has been developed 60 years ago.[30] 2D TMDs are usually formed as thin films rather than single crystals in photoelectrodes due to the fact that 2D TMD thin films can be prepared in large areas and provide efficient absorption of solar light, although 2D TMD thin films have lower quality than monolayer TMDs.[30] For example, Yu *et al.* successfully fabricated self-assembled 2D WSe_2 thin films through the dispersion of solvent-exfoliated few-layer flakes.[111] The thin films with a thickness of *ca.* 25 nm exhibited a sustained p-type photocurrent up to 1.0 mA cm^{-2} at 0 V *vs.* RHE (reversible hydrogen reaction) with an added water reduction catalyst (Pt). The fabrication of thin films provides large-area substrates to absorb a significant region of the solar spectrum to enhance the photoelectrode performance.

In case of increasing the activity of 2D TMDs as photoelectrodes for HER from PEC, 2D TMDs should form heterostructures or composites/hybrids with other materials as photocatalysts or be coated with co-catalysts to effectively separate photoexcited electrons and holes.[112,113] Kwak *et al.* showed experimentally that an Si-based photoelectrode in a nanowire array sheathed in 2D TMD layers achieved a photocurrent density of 30 mA cm^{-2} (at 0 V *vs.* RHE) and high Faradaic efficiency, which reached 90% under AM 1.5G conditions.[114] Also, the HER activity can be enhanced through heteroatom doping. For example, modified 2D TMD-based photoelectrodes, such as a p–n MoS_2/N-doped cGO heterojunction, which exhibited a low overpotential of around 100 mV *vs.* RHE and RGO/CdS/MoS_2 hybrid, have been developed in a previous study.[107] In another study, PEC using Se-doped α-Bi_2O_3 showed a high photocurrent density, high charge carrier density (according to Mott–Schottky plot), lower impedance (by EIS), and low carrier recombination (according to PL spectrum) compared to the pristine α-Bi_2O_3.[115]

2D TMDs show strong potential as photoelectrodes because of their tuneable bandgap, efficient light absorption, and favourable charge transport. However, despite their advantages, 2D TMDs have limited efficiency as photoelectrodes compared to conventional semiconductors. Therefore, progress in thin-film fabrication, heterostructure engineering, and doping will advance their PEC performance for hydrogen generation.

3.2.2 2D TMDs as photocatalysts. Photocatalysts are a family of semiconductor materials, which can absorb solar light to generate free electron–holes to drive catalytic redox reactions on their surface/terminal sites.[109] In general, a photocatalyst operates by absorbing solar light to separate electron–hole pairs and drive redox reactions. When a photon has energy greater than or equal to the photocatalyst bandgap, the electron will be excited from the VB to CB. Depending on the target reaction, electrons may reduce protons into hydrogen (HER) or CO_2 into carbon-based fuels, while holes oxidize water in OER or degrade organic pollutants.

Several semiconductors such as 2D TMDs,[50,116] TiO_2,[117] and g-C_3N_4 (ref. 118 and 119) have been widely utilized as photocatalysts. Several photocatalysts still have limitations due to their restricted light response and unsuitable charge

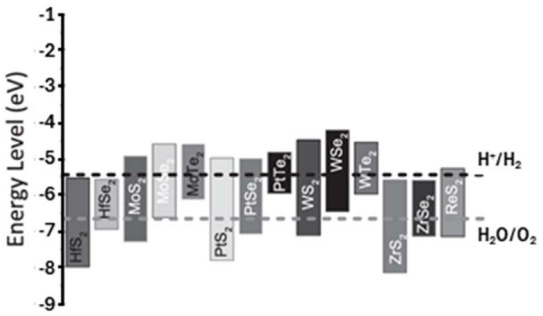

Fig. 7 Band edges of 2D TMDs to generate the HER or OER. Reproduced from ref. 108 with permission from Wiley-VCH Verlag GmbH & Co., copyright 2017.

separation.[120] However, their tuneable band gap across the visible-IR light absorption range, strong light-matter interaction, and long electron–hole recombination time lead to enhance photocatalytic performances, and the flexibility to engineer them such as phase engineering, vdW heterostructure, or Janus heterostructure are advantages of using 2D TMDs as photocatalysts. The purpose of using 2D TMDs as photocatalysts is to minimize the overpotential for the HER, while absorbing solar light to generate electron–hole pairs. Here, layered photoelectrodes using 2D TMDs as photocatalysts aimed to enhance the performance of PEC cells to produce H_2.[121,122] In general, materials can be determined as good HER photocatalysts if they give a value close to 0 eV in terms of Gibbs energy change for H_2 adsorption.[29] Although 2D TMDs have a wide sunlight absorption range, 2D TMDs still have limitations as photocatalysts such as basal planes, which are HER inert and have poor electrical conductivity. Several routes can be used to enhance the catalytic activity of 2D TMDs such as phase engineering, defect engineering, heteroatom doping, and structure engineering.

As photocatalysts, 2D TMDs are used to enhance the PEC performance. 2D TMDs exhibit a high catalytically active surface area and active basal planes to provide a high yield and efficient HER.[123] Given that their catalytic activity is active site/surface dependent, different phases of 2D TMDs show various catalytic activity. Semiconducting 2D TMDs such as 1H/2H and 3R phases have basal planes, which are inert for HER, while the metallic 1T phase has a metallic surface, which is an active site for HER. Phase engineering is a common and simple route to enhance the photocatalytic activity of 2D TMDs.[124] It is important to know that the phase transition from an H phase to T phase and coexisting phases will modulate the electronic properties and active sites, resulting in enhanced catalytic activity. Chang *et al.* successfully synthesized 2H and 1T phase MoS_2. The result showed a phase transition from 2H to high yield and quality 1T phase by annealing at 1000 °C using lithium salt precursor.[50] 1T phase MoS_2 absorbs light in the full spectral range of 300 to 1200 nm efficiently and has an active basal plane as an excellent photocatalyst. The 1T phase has a lower energy level and bandgap, which leads to the easy capture of photo-excited electrons and facilitate HER activities. Mouloua *et al.* combined the properties of 1T and 2H phase MoS_2 by synthesizing the 1T/2H–MoS_2 core/shell structure (Fig. 8a).[125] Here, the 1T phase as a coating provides good conductivity, while the 2H phase ensures excellent and efficient light absorption. Also, it exhibited a fast response (360 ms) to reach the maximum photocurrent density value of 90% (Fig. 8b) and photocurrent density of -13.5 ± 1 A cm^{-2} at 0 V *vs.* RHE at the onset potential of 110 mV (Fig. 8c). Therefore, as a catalyst, 1T MoS_2 has a better photocatalytic performance, as shown by its lower overpotential and high current density. Parallelly, Toh *et al.* compared the 3R and 2H phases of MoS_2 and WS_2 for HER photocatalytic activity and showed that the 3R phase of MoS_2 and WS_2 minimizes the overpotential for HER in PEC, which exhibited a better photocatalytic performance than the 2H phase.[51] It is clear that the 3R phase of MoS_2 was formed as a mixture with the 3R phase, and higher 3R phase concentrations resulted in superior HER efficiency. Also, they found that the performance is particle crystal size dependent. Various phase engineering of 2D TMDs with nanosheet structures and varying synthesis methods have also been developed to evaluate the HER performance through the overpotential value (Fig. 8d). The amount of layer could trigger a phase transition that affects the photocatalytic activity. However, in the case of ReS_2, the amount of stacking layers had no effect on its photocatalytic activity and its 1T natural stable phase exhibited high active sites.[109]

Typically, transition metal diselenides have higher catalytic activity compared to their disulfide counterparts for the same transition metal atom. A study showed that Se has higher metallic property than S, also including other properties and performances such as metallic binding with transition metals, metallic binding to transition metals, and electroactive unsaturated centers, but smaller band gap.[29] Jameel *et al.* showed a comparison of the bandgap between diselenides and disulfides for W, Pt, and Mo metal atoms.[128] In the energy band gap comparison, WS_2, PtS_2, and MoS_2 exhibited values of 1.96 eV, 1.62 eV, and 1.50 eV, while WSe_2, $PtSe_2$, and $MoSe_2$ had values of 1.34 eV, 0.88 eV, and 0.74 eV, respectively.[128] Transition metal diselenides create extra gamma active sites that build extra CB and VB, thus reducing the bandgap. This implies that for the same metal atoms and conditions, transition metal diselenides are expected to efficiently absorb a wide solar spectrum. Gholamvand *et al.* performed a comparison of HER activity in acidic media, showing that selenide has the best HER activity among chalcogenides, followed by sulfide and telluride.[129] Nevertheless, $MoSe_2$ has low water absorption in alkaline solutions. Several approaches can be employed to enhance the HER performance of $MoSe_2$, such as forming hybrids with more conductive materials, including carbon-based materials (CNTs, graphene, MXenes, and g-C_3N_4).

Besides H_2 evolution, PEC water splitting also involves the OER, and thus a photocatalyst must exhibit high stability under high potential conditions, specifically >1.23 V *vs.* SHE (standard hydrogen electrode). Although $MoSe_2$ demonstrates good HER activity, $MoSe_2$ and other typical transition metal diselenides suffer from poor stability in OER. Thus, to address this issue, heteroatom doping can be employed, such as Cu_2S nanocrystal-decorated $MoSe_2$ and Co/Ni nanoparticles as co-catalysts.

Defects and crystal vacancies play a big role in improving the photocatalytic activity of 2D TMDs. The photocatalytic activity of 2D TMDs can be improved by employing chalcogenide vacancies, for example S and Se vacancies given that S and Se are the most typical chalcogenides in 2D TMDs. Son *et al.* engineered poor electrical 2H–MoS_2 by activating its basal plane through the introduction of high doping V atoms.[130] The experiment showed that high V-doped MoS_2 has a superior HER performance, which give an overpotential of 100 mV at 10 mA cm^{-2}. Furthermore, the catalytic performance can be proportionally proven by determining the double-layer capacitance (C_{dl}) value. Single-atom-doped (SAD) V in MoS_2 shows (C_{dl}) up to 45.61 mF cm^{-2} over coalescent-doped (CD) and pristine MoS_2. In the case of 2D InSe, Huang *et al.* showed that the highest catalytic activity was found at the vacancy of four-layer InSe,

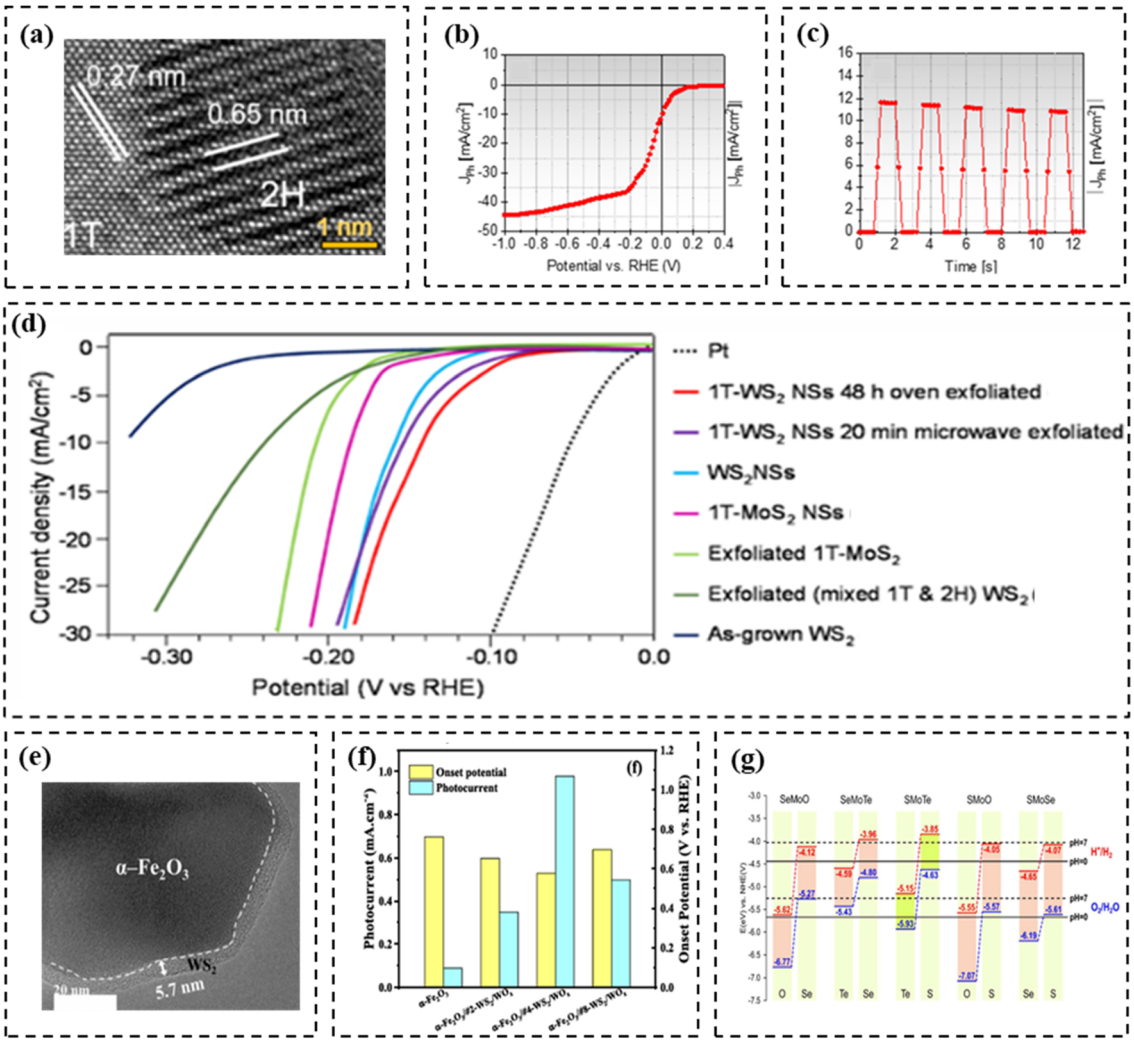

Fig. 8 (a) Structure of 1T/2H–MoS_2 core/shell, (b) chronoamperometry experiments conducted under standard solar irradiation at 1 second dwell time for 5 consecutive cycles, and (c) photocurrent density *vs.* potential. Reproduced from ref. 126 with permission from Elsevier, copyright 2025. (d) Photocurrent density *vs.* potential (V *vs.* RHE) for Pt, WS_2, and MoS_2 for various phases and synthesis methods. Reproduced from ref. 127 with permission from Hydrogen Energy Publications LLC, copyright 2022. (e) Core shell structure of α-Fe_2O_3/4#-WS_2/WO_x and (f) photocatalytic performance with 0, 2, 4, and 8 WS_2 layers. Reproduced from ref. 125 with permission from Elsevier, 2022. (g) Band gaps of various Janus 2D TMDs (SeMnO, SeMoTe, SMoTe, SMoO, and SMoSe). Reproduced from ref. 127 with permission from Hydrogen Energy Publications LLC, copyright 2022.

which is ~30× higher than that on the basal plane.[131] This indicates that defects and crystal vacancies can be introduced to increase the number of active sites on the basal plane and enhance the electrical conductivity, thereby increasing the photocatalytic performance.

Structure engineering is a typical modification of 2D TMD layered photoelectrodes to increase their PEC performance by providing more edge site towards the enhancement of HER performance. Structure engineering can be achieved through TMD/TMD heterostructures or TMD/non-TMD heterostructures *via* the typical vdW heterostructure.[132] Additionally, Janus structures and heterostructures in TMDs can further improve their HER activity.[29] A heterojunction between TMDs as the catalyst and the photoelectrode will decrease the onset potential to lower the applied voltage.[125] In a previous study, engineering the structure of 2D TMDs has been successfully performed, such as the fabrication of MoS_2/rGO hybrid, MoS_2/mesoporous graphene foam (MGF) heterostructure, WS_2 nanosheets/rGO, $W_xMo_{1-x}S_2$/graphene, $MoS_2/CoSe_2$, $CoS_2/CoSe_2$, and $MoSe_2$/NiSe.[133] Masoumi *et al.* successfully synthesized core–shell α-Fe_2O_3/WS_2/WO_x by employing WS_2 nanosheets on an α-Fe_2O_3 nanorod photoanode to make a heterojunction structure with the additional formation of WO_x (WO_4^-, WO_3^-, WO_2^-, and WO^+ ions) on the top surface as a protection layer.[124] This resulted in the formation of α-Fe_2O_3/4#-WS_2/WO_x (Fig. 8e), which means it required 4 times the amount of WS_2 on the α-Fe_2O_3 top surface, exhibiting a photocurrent density about 13- and 30-fold higher compared to pure α-Fe_2O_3. α-Fe_2O_3/4#-WS_2/WO_x gave a photocurrent density of 0.98 and 2.1 mA cm^{-2} (at 0.54 and 0.47 V *vs.* RHE) under front and back illumination, respectively, also at

1.23 V *vs.* RHE under 100 mW cm^{-2} (Fig. 8f). Therefore, core–shell structures can be implemented to effectively separate and prolong the recombination time of electron–hole pairs to enhance the PEC performance.

Further, the study by Li *et al.* showed the fabrication of $MoSe_2$–CdS–ZnS tandem Z-scheme heterojunction arrays with ultrathin $MoSe_2$ nanosheets anchored on CdS–ZnO nanorods on an Au paper working electrode (Au-PWE) to enhance PEC water splitting. Consequently, the photocurrent density reached up to 2.4 mA cm^{-2} at 0.3 V *vs.* the normal hydrogen electrode (NHE).[69] In other research, H phase Janus 2D structures of TMDs composed of O, S, Se, and Te atoms have been successfully fabricated, and their band alignment compared to the redox potential is shown in Fig. 8g. SMoTe is a promising candidate because of its sustainability in both acidic and neutral media.[127] Moreover, MoSSe is a Janus 2D TMD that can be considered a photocatalyst due to its higher photocatalytic properties (including optical absorption, carrier mobility, and H_2O absorption) compared to the conventional MoS_2 photocatalyst.[134] The catalytic activity and HER performance of MoSSe are structure and stacking sequence dependent, similar to typical 2D TMDs.[135] In another new study reported by Xiong *et al.*, they successfully fabricated MoSSe/Bi_2WO_6 with S-scheme heterojunction construction to provide a novel strategy to enhance the catalytic performance.[136] The light absorption capacity of MoSSe/Bi_2WO_6 is in the range of 20–29% and its photocurrent density reached up to 4.54 mA cm^{-2} at 2 V *vs.* RHE. In the heterojunction, MoSSe provides a large specific surface area and excellent reduction potential, emerging as an ideal carrier to load other materials. The construction of a heterojunction has become a simple and common way to enhance the photocatalytic performance of 2D TMDs.

Despite their promising photocatalytic activity, 2D TMDs such as MoS_2, $MoSe_2$, WS_2, and WSe_2 still face challenges when employed as photoelectrodes or photocatalyst. To this end, the 2H phase is thermodynamically the most stable.[31] However, the 1T phase generally exhibits a superior photocatalytic performance. Consequently, various engineering approaches are required to enhance the photocatalytic performance of the 2H phase or to improve the stability of the 1T phase. Furthermore, 2D TMD thin films often suffer from poor long-term stability during the PEC process due to their large interlayer spacing and intrinsically weak vdW structures.[30] During the PEC reaction, the vdW structures can be easily penetrated by the electrolyte species, which lead to intercalation that weakens the heterostructure contacts and promotes the formation of pinholes and cracks.[30] Thus, although heterostructure engineering is widely used to improve the electronic and optoelectronic properties of 2D TMDs, it still has inherent limitations in terms of structural stability.

However, 2D TMDs have demonstrated great promise as photocatalysts for PEC H_2 evolution owing to their tuneable bandgaps, broad solar absorption (300–1200 nm for 1T–MoS_2), and highly active metallic phases. Phase engineering has shown that 1T–MoS_2 exhibits superior catalytic activity compared to 2H, delivering photocurrent densities up to −13.5 A cm^{-2} at 0 V *vs.* RHE with low overpotentials, while the 3R phases of MoS_2 and WS_2 outperform their 2H counterparts by minimizing the HER overpotentials. Selenides such as $MoSe_2$ and WSe_2 generally exhibit higher photocatalytic activity than sulfides (MoS_2 and WS_2), although their stability in OER remains a challenge. Further improvements have been achieved through defect engineering (V-doped MoS_2 showing overpotentials of around 100 mV at 10 mA cm^{-2}) and heterostructure formation (*e.g.*, MoS_2/rGO and $MoSe_2$/NiSe), with the $MoSe_2$–CdS–ZnS heterojunction giving a photocurrent density of around 2.4 mA cm^{-2} at 0.3 V *vs.* NHE. These findings collectively highlight that phase modulation, doping, and heterostructure construction are crucial strategies to unlock the full photocatalytic potential of 2D TMDs for sustainable H_2 generation.

3.2.3 2D TMDs as co-catalysts. Semiconductor materials are frequently used as photocatalysts in PEC water splitting for HER. Typically, the employment of a photocatalyst does not result in a high catalytic performance for HER due to the fast electron–hole recombination time.[137] In this case, 2D TMDs are now promising co-catalysts frequently used in PEC water splitting to enhance HER.[138–141] As co-catalysts, 2D TMDs serve to capture excited electrons in the CB to efficiently separate them from the holes and provide more active sites. The efficient capture of electrons and high active sites are two important things to enhance the photocatalytic HER activity.[142] Also, several modifications can be utilized to further enhance the performance of 2D TMDs as co-catalysts, such as the fabrication of heterojunctions of 2D TMDs and phase engineering, which can prolong the electron–hole pair recombination time and increase the interlayer transport efficiency. Both the 1T and 2H phases are the most common phases in 2D TMDs utilized as co-catalysts. However, in terms of co-catalyst application, the 1T phase is known to provide more active sites for H_2 generation, where the general 2H phase is catalytically inert.[142] Activation of the basal plane could be another option to serve higher active sites for enhancing H_2 generation. Yu *et al.* employed Mo doping to activate inert S atoms by acting as electron donors and modulating the p-band center of adjacent S atoms.[143] Roy *et al.* showed that activating the basal plane of MoS_2 by heterostructuring with $MoSe_2$ results in a photocurrent density of 19.35 mA cm^{-2} and incident photon-to-current efficiency (IPCE) of 38.4%, which is 1.2- and 1.36-times higher compared to those of pristine MoS_2 on Si nanowires, respectively.[144] Another method that can be used to enhance the photocatalytic performance is the use of thin films. Thin films of 2D TMDs can act as stabilizers for electrode/semiconductor photocatalysts by preventing the photogenerated holes from attacking or corroding the electrode.[98]

Various 2D TMDs have been developed and employed to enhance the photocatalytic performance. Yi *et al.* designed the utilization of 1T-WS_2 as a co-catalyst for 2D-C_3N_4 semiconductor for H_2 generation and compared its performance with the 2H phase.[142] The photocurrent density measurement over time at a bias potential of −0.2 V *vs.* Ag/AgCl under visible light irradiation, as shown in Fig. 9a, shows that the 1T phase exhibits a higher photocurrent density compared to the 2H phase and non-co-catalyst 2D-C_3N_4. This implies that the 1T phase more efficiently separates electrons from holes and prolongs the

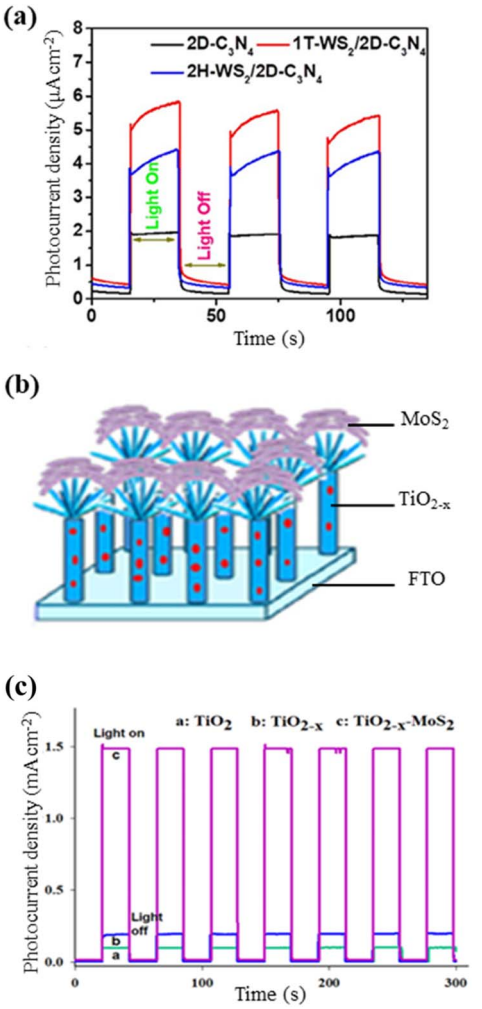

Fig. 9 (a) Photocurrent measurement over time of 1T and 2H phase WS_2 on 2D-C_3N_4 and pristine 2D-C_3N_4. Reproduced from ref. 142 with permission from Elsevier, copyright 2017. (b) Structure illustration of TiO_{2-x}-MoS_2/FTO and (c) photocurrent–time profiles of TiO_2, TiO_{2-x}, and TiO_{2-x}–MoS_2 in 0.5 M Na_2SO_4 under dark and light conditions. Reproduced from ref. 147 with permission from The Korean Society of Industrial and Engineering Chemistry, copyright 2024.

electron–hole recombination time. Also, the amount of 15% 1T-WS_2 gave the optimal performance to enhance H_2 production under visible light irradiation.[142] The utilization of ReS_2 by Jing *et al.* resulted in a higher photocatalytic performance in TiO_2, which had a higher photocurrent density over time compared to the pristine TiO_2.[145] The 1T distorted phase of ReS_2 establishes good absorption in the entire visible light region, which is suitable for solar energy harvesting. Moreover, the heterojunction between ReS_2 and TiO_2 prolongs the electron–hole pair recombination time and increases the amount of excited electrons. Therefore, the excited electrons can be utilized effectively. Besides the application of MoS_2 as a photocatalyst, the 2H phase of MoS_2, which possesses a basal plane, exhibits excellent catalytic activity when utilized as a co-catalyst for CdS or other typical semiconductors with a higher CB position.[50] If a Z-scheme heterojunction is constructed, the excited electrons can be exploited to produce H_2 efficiently.[146] Rezaei *et al.* used TiO_{2-x}–MoS_2 to enhance the visible light absorption and improve the PEC performance by accelerating the separation of photogenerated excitons and restricting the recombination of electrons and holed in an FTO photoanode (Fig. 9b). The presence of TiO_{2-x}–MoS_2 resulted in a photocurrent density of 1.4 mA at 1.23 V *vs.* RHE and the photocurrent measurement with time is shown in Fig. 9c.[147] Also, Wang *et al.* showed that the integration of an MoS_2 layer on GaN, which formed MoS_2/GaN vdW heterojunctions, resulted in wider visible-light absorption compared to the pristine GaN, as depicted in Fig. 10a.[148] The formation of MoS_2/GaN resulted in a moderate bandgap (1.35–1.7 eV), which is thickness dependent. The integration of MoS_2 with GaN can overcome the issue of the GaN heterojunction due to the lattice mismatch. Further, MoS_2/GaN exhibited large and wide visible light absorption, which is suitable for photocatalyst applications. In a recent study by Degg *et al.*, they formed a composite tin iodine phosphide (SnIP) photocatalyst with $MoSe_2$ and MoS_2 to achieve multiple PEC responses.[149] The potential (in V *vs.* RHE) *versus* the applied bias photon-to-current efficiency (ABPE) graphs in Fig. 10b and c show that only $MoSe_2$ exhibits an effect as a co-catalyst to increase the PEC performance with the photocurrent density of 0.025 mA cm^{-2} at 0.8 V *vs.* Ag/AgCl. This is consistent with the previous discussion that compares transition metal diselenides and disulfides in 2D TMDs in the photocatalyst subsection. A similar trend is also observed when 2D TMDs are used as co-catalysts, where transition metal diselenides, here $MoSe_2$, exhibit superior co-catalytic effects compared to their disulfide counterparts. The utilization of $MoSe_2$ and MoS_2 to enhance the PEC performance was also carried out by Ali *et al.*, which constructed 5 wt% $MoSe_2$–MoS_2/ZnO. The utilization of $MoSe_2$–MoS_2 on ZnO resulted in a 2-fold higher photocurrent than the pristine ZnO, which shows that the utilization of $MoSe_2$–MoS_2 can enhance the photoelectrode performance.[150] Further, the performance of $MoSe_2$–MoS_2/ZnO can be enhanced by 3-fold that of pristine ZnO by heterostructuring with 2.5 wt% Te-rich $MoTe_2$. Here, the higher electrical conductance and field effect of Te-rich $MoTe_2$ than $MoSe_2$ and MoS_2 play a role in enhancing the efficient transport of photoexcited charge carriers.[151] Another experiment by Li *et al.* demonstrated the use of $PtSe_2$ as a co-catalyst of SiC with a vdW heterostructure scheme.[152] Adding $PtSe_2$ as a co-catalyst resulted in higher light absorption (Fig. 10d) and higher solar to hydrogen (STH) efficiency compared to other heterostructure materials (GeS/GeSe, g-C_6N_6/InP, GeH/InSe, and GaAs/InS) (Fig. 10e). In the diagram, the STH value slightly decreases from 34.7% to 31.21%, 27.32%, 24.72%, and 17.06% for SiC/$PtSe_2$, GeS/GeSe, g-C_6N_6/InP, GeH/InSe, and GaAs/InS, respectively.

The Te site in the MTe_2 family, especially the 1T′ phase, is believed to be the adsorption site for hydrogen atoms, and thus the reaction site for HER. However, the MTe_2 family is mostly used in electrochemical HER rather than photocatalytic HER. This is because the position of the CB of most MTe_2 is not suitable for driving HER.[153] Moreover, the MTe_2 family exhibits a strong exciton binding energy, indicating that electron–hole pairs are difficult to separate, limiting their ability to participate

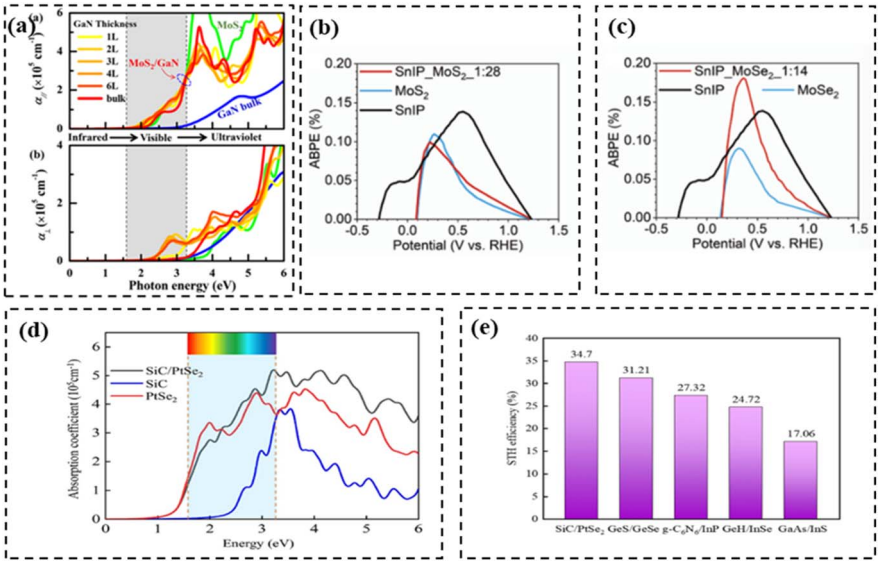

Fig. 10 (a) Optical absorption spectra of an MoS_2/GaN heterostructure with different GaN thicknesses along in-plane (top) and out-of-plane (bottom). Reproduced from ref. 148 with permission from the American Chemical Society, copyright 2019. ABPE in percent *versus* potential (V *vs.* RHE) of SnIP composite with (b) 1 : 28 and (c) 1 : 14 composition of SnIP : MoS_2. Reproduced from ref. 149 with permission from Wiley-VCH Verlag GmbH & Co., copyright 2025. (d) Optical absorption coefficient of SiC, $PtSe_2$, and SiC/$PtSe_2$ and (e) comparison of STH efficiencies of SiC/$PtSe_2$ and other heterostructures. Reproduced from ref. 152 with permission from Elsevier, copyright 2024.

in light-driven reactions.[154] The current state of the art shows that only $NiTe_2$ and $MoTe_2$ have been used for photocatalytic HER in the MTe_2 family. There has been no report on the use of $MoTe_2$ and $NiTe_2$ alone as a photocatalyst for driving HER. Most research focuses on combining $MoTe_2$ and $NiTe_2$ with different materials to form a heterostructure. In this trend, a common agreement has not been established yet given that only a few studies are present. In one case, it was proposed that $NiTe_2$ serves as an oxidation photocatalyst, helping the separation of electron–hole pairs in g-C_3N_4, which drive the actual HER.[155] Other than its combination with g-C_3N_4, another research group enhanced the charge separation in $NiTe_2$ by decorating Ni nanoparticles on its surface. As a result, the HER performance increased by ~1.55 times compared to single $NiTe_2$.[156]

2D TMDs serve as highly effective co-catalysts in PEC water splitting by capturing photogenerated electrons, suppressing charge recombination, and providing abundant catalytic sites. Phase engineering, basal-plane activation, and heterostructure formation have demonstrated substantial improvements in photocurrent density and efficiency, such as MoS_2/$MoSe_2$ reaching 19.35 mA cm^{-2} with an IPCE of 38.4%, and 1T-WS_2/2D-C_3N_4 showing a superior H_2 production compared to its 2H counterpart. These results highlight that co-catalyst integration not only enhances the charge transfer and stability of semiconductor photoelectrodes but also unlocks the full catalytic potential of 2D TMDs for efficient H_2 generation. Several applications of 2D TMDs along with their synthesis method and phase are shown in Table 1.

Table 1 2D TMDs for H_2 production

Synthesis method	System	Phase	Condition	Performance	Ref.
Chemical intercalation	MoS_2/TiO_2	2H	Visible light	Photocatalytic H_2 activity: 5 μmol h^{-1}	
		1T		Photocatalytic H_2 activity: 228.2 μmol h^{-1}	
	MoS_2/CdS	2H		Photocatalytic H_2 activity: 1563.6 μmol h^{-1}	50
		1T		Photocatalytic H_2 activity: 1658.5 μmol h^{-1}	
Chemical vapor deposition (CVD)	MoS_2/Si	1T/2H	450 nm light	Photocurrent density: −13.5 ± 1 mA cm^{-2}	126
				Onset potential: 0.11 V *vs.* RHE	
Hydrothermal	Co-WS_2/$Cd_{0.4}Zn_{0.6}S$	2H	Visible light	Photocatalytic H_2 activity: 21 000 μmol g^{-1} h^{-1}	157
	WS_2/2D-C_3N_4	1T	300 W Xenon lamp	Photocatalytic H_2 activity: 331.09 μmol g^{-1} h^{-1}	142
		2H		Photocatalytic H_2 activity: 171.51 μmol g^{-1} h^{-1}	
	$MoSe_2$/CdSe	1T/2H	Visible light	Photocatalytic H_2 activity: 7.12 mmol g^{-1} h^{-1}	158
	Te–$MoTe_2$–MoS_2/ZnO	2H		Photocatalytic H_2 activity: 5.2 mmol cm^{-2} h^{-1}	151
	$MoSe_2$–MoS_2/ZnO	2H		Photocatalytic H_2 activity: 7.43 mmol cm^{-2} h^{-1}	150
	MoS_2-BN/TiO_2	2H		Photocatalytic H_2 activity: 2.6 μmol cm^{-2} h^{-1}	146

3.3 Clean fuel production from CO_2 photoreduction

Climate change, especially global warming, is currently a hot topic of challenges in environmental studies. Both the global sea surface temperature and upper 2000 m ocean heat content record reached the highest temperature in 2024, and the 12-month average also reached its highest point in August 2024 at 1.6 °C above the recorded temperature at the start of the last century.[159,160] The occurrence of global warming cannot be separated from the greenhouse effect. Most of the GHG was CO_2, which contributes around 76% to the total greenhouse emissions besides methane (16%), nitrous oxide (6%), and other gasses.[161] One of the promising strategies to overcome this environmental problem is photoreduction, converting CO_2 to C_1 or C_{2+} products, which are more usable chemicals such as carbon monoxide (CO), methane (CH_4), methanol (CH_3OH), and ethanol (C_2H_5OH).[162,163] Compared to C_1 products from CO_2 photoreduction, C_{2+} products exhibit a higher energy density and broader application.[164]

The clean energy obtained from photoreduction methods can also be a solution to the energy problems besides overcoming environmental problems by reducing CO_2 levels.

Various catalysts have been fabricated from semiconductors to reduce CO_2. Unfortunately, they exhibit limitations such as unstable conditions, insufficient photocatalytic activity, and inadequate productivity.[19] Several strategies have also been developed to overcome these drawbacks, including adding noble metal co-catalysts, increasing the porous structure surface area, and employing appropriate band architectures.[165] It is essential to increase the efficiency of CO_2 reduction by using photocatalysts, where solar energy drives the redox reaction to reduce CO_2 with broad-range absorbance in the ultraviolet (UV), visible (vis), and near-IR light regions.[19,166] The structures that can improve solar light absorption and absorb UV-vis to IR radiation are materials with 2D structures.[167] 2D materials also facilitate the mobility of electrons, reducing the band gaps and thermal conductivity.[167] Among the photocatalyst candidates, 2D TMDs are potential candidates due to their excellent electrocatalytic properties, low cost, abundant reserves on Earth, and ability to convert CO_2 efficiently at relatively low temperatures.[14,168] This section discusses the application of several 2D TMDs (MoS_2, $MoSe_2$, WS_2, WSe_2, $MoTe_2$, WTe_2, and $NiSe_2$) in clean energy production by CO_2 photoreduction.

3.3.1 Molybdenum disulfide (MoS_2). MoS_2 is a layered metal chalcogenide with semiconductor characteristics.[169] MoS_2 exists in three different phases, *i.e.*, 1T phase with tetragonal symmetry, 2H phase with hexagonal symmetry and octahedral coordination of Mo atoms, and 3R phase with rhombohedral structure of three layer S–Mo–S.[170] Owing to its absorbance capabilities in the near-IR band, MoS_2 has been extensively explored to support the photocatalytic performance.[167] For instance, a 2D structure of MoS_2 sheet has been explored to produce CH_3OH and acetaldehyde by CO_2 photoreduction.[170] When UV light irradiated MoS_2, electrons transferred from VB to CB, which induced fast transitions of photogenerated electrons, resulting in a decrease in charge carrier recombination.[171] The mechanism of this photocatalytic performance is illustrated in Fig. 11a. MoS_2 has also been explored to increase the photocatalytic activity of semiconductors, such as ZnO, by modifying their surface-bound active species to extend their light absorption capabilities. Li *et al.* utilized MoS_2 and In_2O_3 to modify the surface of ZnO to improve its photoelectric properties and band structure, potentially enabling the production of CO and CH_4 from CO_2. Firstly, CO_2 is reduced to CO as an intermediate product, which is then further reduced to CH_4 as the final product. The photocatalytic activity of ZnO and its combination with In_2O_3 and MoS_2 for CO and CH_4 production can be seen in Fig. 11b. In this example, the electrons in the CB of In_2O_3 and MoS_2 are excited to the VB, producing photogenerated electron and holes. The photogenerated holes in ZnO migrate to the VB of In_2O_3, whereas the photogenerated electrons from In_2O_3 and the CB of ZnO transfer to the CB of MoS_2. The surface of ZnO can used as transfer channels due to the surface-bound active species by In_2O_3 and MoS_2, facilitating electron–holes transfer to the surface of the catalysts. This enhanced charge separation and transfer increases the production of CO as an intermediate and CH_4 as the final product.[165]

Although MoS_2 has been chosen to be an effective candidate to reduce CO_2, it poses several limitations such as poor conductivity, poor stability, and propensity for photo corrosion.[173] Its photocatalytic activity can be improved by combining two TMDs, MoS_2 and SnS_2, which provide rich functional active sites. A composite of rGO-MoS_2 and SnS_2 was shown to produce CO and CH_4 under UV light. The presence of SnS_2 improved the synergistic effects to increase the photocatalytic activity, and it was also shown that its combination with rGO boosted the number of usable excitons and charge carriers.[173] The yield of CO by MoS_2 only is 1.98 μmol g^{-1}, which increased to 113.97 μmol g^{-1} when combined with 3% rGO and 342.66 μmol g^{-1} when combined with 10% SnS_2. The increasing yields were also shown in the production of CH_4, with 1.15 μmol g^{-1}, 81.61 μmol g^{-1}, and 252.74 μmol g^{-1} for MoS_2, MoS_2-3% rGO, and MoS_2–10% SnS_2-3% rGO, respectively.[173]

The photocatalytic performance also can be improved by combining two materials with different bandgaps to produce a heterostructure. For example, the combination of NiFe-layered double hydroxide (LDH) and MoS_2 with different bandgaps of 2.42 eV and 1.86 eV, respectively.[174] Sunlight irradiation induces photon excitation to produce electron–hole pairs in the catalyst and the possible electron transport pathways with these two different energy bands are type-II and direct Z-scheme, as shown in Fig. 12a. In the type-II heterojunction, the holes from MoS_2 would transfer to NiFe-LDH and the electrons from the CB of NiFe-LDH would transfer to MoS_2. The reduction of CO_2 to CO is difficult because its reduction potential is −0.53 V and the strongest reduction oxidation capacity was lost, which did not exhibit effective photocatalytic CO_2 reduction ability after their combination. Thus, a direct Z-scheme heterojunction is a better way for understanding the electron transport mechanism. The electron from the conduction band is excited to the VB of MoS_2. The heterojunction facilitates the separation of the electron–hole pairs that easily

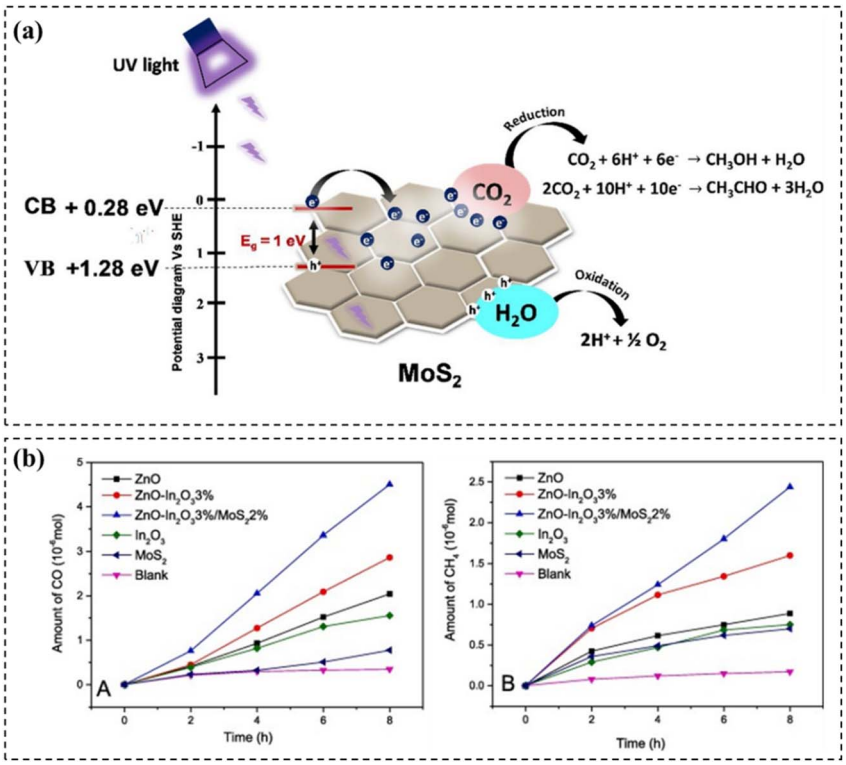

Fig. 11 (a) Mechanism of photocatalytic performance of MoS_2 to produce methanol and acetaldehyde. Reproduced from ref. 170 with permission from Elsevier, copyright 2019. (b) Production of CO and CH_4 for 8 h under UV light irradiation using ZnO, In_2O_3, MoS_2, and their combinations. Reproduced from ref. 172 with permission from Elsevier, copyright 2021.

reunite. With the direct Z-scheme heterojunction, oxidation and reduction reactions can be conducted at the most positive and negative energy band positions to successfully encourage the separation of photogenerated carriers.

3.3.2 Molybdenum diselenide ($MoSe_2$). $MoSe_2$ is a TMD material with the thermodynamically stable 2H phase but poor conductivity. This material is usually used as a photocatalyst because it has an excellent photocatalytic response on its 1T phase.[168] The hybrid phase of 1T-2H $MoSe_2$ has been explored in combination with Cu and TiO_2 nanofibers (NFs) for CO_2 photoreduction. CO_2 was converted to H_2, CO, and CH_4 gases, as can be seen in Fig. 12b. The doping of Cu on TiO_2 NFs improved their poor catalytic performance than pure TiO_2 but still showed poor selectivity for H_2 gases. A coating using $MoSe_2$ was reported to be optimum at 2 wt% concentration, as indicated by the yield of CO of 396 μmol g^{-1}; H_2 of 81 μmol g^{-1}; and CH_4 of 92 μmol g^{-1}. $MoSe_2$ was hydrophobic in nature, limiting the sample contact with water, and it created more active sites for the adsorption of CO_2 and intermediates, resulting in an improvement in charge separation compared to the sample without $MoSe_2$. Fig. 12c illustrates the mechanism of charge transfer for 2 wt% $MoSe_2$ on Cu–TiO_2 NFs under UV-visible light. The contact of Cu–TiO_2 NFs with $MoSe_2$ resulted in electron transfer from $MoSe_2$ to the composite of Cu–TiO_2 NFs, causing an electron field from the TMDs to Cu–TiO_2 and band bending at their interface. The reduction of CO_2 was maintained in the CB of $MoSe_2$, while in Cu–TiO_2, the weak photoexcited electrons in its conduction band combined with the weak photoexcited holes in its VB, which were encouraged by the electron field and band bending. The spatial separation of photogenerated electron–hole pairs was greatly enhanced by S-scheme charge transfer.[168]

The yield of CO_2 conversion can be enhanced by increasing the number of active sites and the surface area. Jiang *et al.* introduced the combination of CeO_2 and $MoSe_2$ in a hollow frame structure enriched with oxygen vacancies, which significantly improved the CO_2 adsorption capacity.[173] As shown in Fig. 12d, CO_2 reduction to yield CH_4 gases on CeO_2-49.7 wt% $MoSe_2$ with high oxygen vacancies required a negative desorption energy (−0.39 eV), indicating that the process is in a spontaneous oxygen-rich-environment. Hollow structures also have been utilized to improve the photocatalytic performance in $CuIn_5S_8$–$MoSe_2$ containing sulphur vacancies. The cavity in hollow structures leads the multiple light reflections to improve the efficiency of light utilization. The CB positions of $CuIn_5S_8$ with sulphur vacancies and $MoSe_2$ are −0.72 eV and −1.1 eV, respectively. Both are more negative than the reduction potentials of CH_4 and CO, indicating favourable conditions for enhanced photocatalytic CO_2 reduction.[176]

3.3.3 Tungsten disulfide (WS_2). WS_2 is a two-dimensional transition metal dichalcogenide with visible/near IR activity.[177] WS_2 exhibits more active sites on its basal plane and edges of its 1T metallic phase, while its 2H phase is thermodynamically stable, which is favorable for CO_2 reduction. The

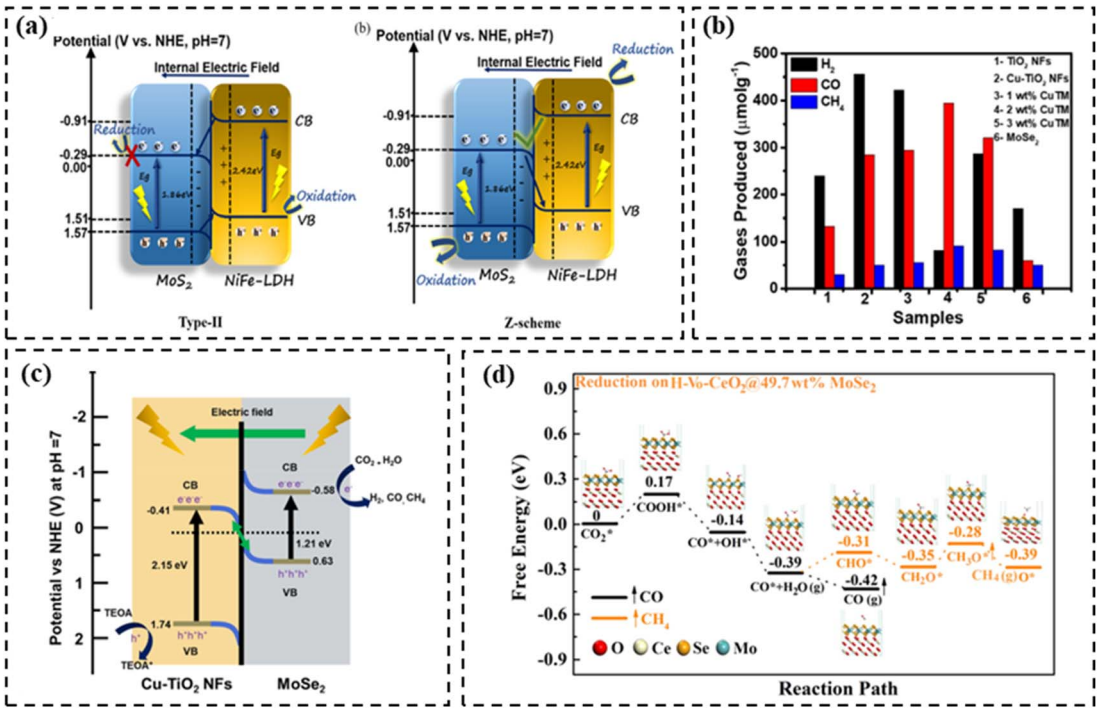

Fig. 12 (a) Illustration of the electron transport pathways in type-II and Z-scheme heterojunctions. Reproduced from ref. 175 with permission from Zhou *et al.*, copyright 2024. (b) Production of gas by $MoSe_2$ coatings on Cu–TiO_2 NFs. Reproduced from ref. 168 with permission from Elsevier, copyright 2023. (c) Charge transfer mechanism on the Cu–TiO_2 NF–$MoSe_2$ composite for CO_2 photoreduction. Reproduced from ref. 168 with permission from Elsevier, copyright 2023. (d) Reaction path and free energy diagram of CeO_2-49.7wt%$MoSe_2$ with high oxygen vacancy to produce CO/CH_4 from CO_2. Reproduced from ref. 175 with permission from Elsevier, copyright 2021.

homoconjunction of 1T/2H WS_2 can be favorable for the formation of CH_4 from CO_2. Zhou *et al.* reported the homoconjunction of 1T/2H WS_2 in combination with TiO_2. The CO_2 photoreduction performance of 1T/2H-WS_2/TiO_2 in producing CH_4 under a 300 Xe lamp is 36.44 μmol g^{-1} h^{-1}, which is 12.8-times higher than pristine TiO_2.[178] Enhanced photoreduction activity can be achieved by combining WS_2 and In_2S_3, which produced 188.6 μmol CH_4 during 12 h reduction of CO_2 under visible light.[177] The effective carrier transfer and layered structure assist electron mobility, leading to an increase in CO_2 reduction activity.[177] WS_2 nanosheets containing sulphur vacancies can be deposited with single metal atoms such as Cu, Co, Pt, Ni, and Pd. The attachment of single metal atoms resulted in promising catalysts for reducing CO_2. For instance, WS_2 doped with Cu and Co showed good potential to produce formic acid and CO. In CO_2 reduction, Cu- and Co-doped WS_2 show an extra hybridization effect between the Co and Cu 3d and W 5d orbitals, respectively, increasing the electron overlap close to the Fermi level and accelerating the charge transfer kinetics.[179]

3.3.4 Tungsten diselenide (WSe_2). WSe_2 is the main 2D TMD with luminescent properties.[180] WSe_2 exhibits the lowest CB among materials, indicating its prospect in energy conversion.[180] The band gap of WSe_2 can directly change according to the wavelength of sunlight when its crystal structure changes from bulk to single layer, indicating its potency in photoelectrocatalytic conversion applications.[181] An increase in the gas yield of CO_2 photoreduction can be achieved by increasing the specific surface area of WSe_2 to provide more active sites. The photon energy induces electron transfer from VB to CB, generating electron–hole pairs. The holes drive the oxidation of H_2O to hydrogen ions, while electrons reduce CO_2 to CH_3OH. The yield of CO_2 photoreduction using WSe_2 can be improved by decorating the surface of WSe_2 with noble metals. The deposition of noble metals will form a metal–semiconductor heterojunction and induce the localized surface plasmon resonance effect. For instance, the surface decoration of WSe_2 with Ag can increase its CO productivity to 14.80 μmol g^{-1} h^{-1} from 5.24 μmol g^{-1} h^{-1}. The photogeneration of electron–hole pairs in Ag/WSe_2 occurs when it is irradiated with visible light. Electrons jump to the conduction band of WSe_2, and eventually to the Ag nanoparticles, contributing to the CO_2 reduction reaction for CO evolution. The CO production remained stable after five cycles, indicating a stable photocatalytic process with time.[182]

3.3.5 Molybdenum ditelluride ($MoTe_2$). $MoTe_2$ is a co-catalyst with a superior photo response and adjustable band gap.[183] $MoTe_2$ is usually applied in industry owing to its excellent transport capacity and metallic conductivity.[184] In the conversion of CO_2, its selectivity can be increased by designing Mo–S bridging bond sites in $MoTe_2$. For example, in Sv-In_2S_3@2H–$MoTe_2$, the Mo–S bridging bonds facilitate the higher adsorption of CO_2 through the strong interaction of CO_2 with Mo. The conversion of CO_2 produced CH_4 with selectivity

Table 2 Products from CO_2 conversion using 2D TMDs as catalysts

TMD	Type	Condition	Parameter	Value	Ref.
NiFe-LDH-MoS_2	Photocatalytic (PC)	300 W, Xe light	CO yield in 4 h (μmol g^{-1})	10.72	174
Cu–S–MoS_2 3%			CO yield (μmol g^{-1} h^{-1})	0.48	188
WSe_2-graphene-TiO_2	PC	UV-visible light	CH_3OH yield (μmol g^{-1} h^{-1})	6.3262	189
WSe_2-graphene				5.0278	26
WSe_2 ($NaBH_4$)	PC	300 W, Xe light	CH_3OH yield in 12 h (μmol g^{-1})	46.32	181
WSe_2 ($N_2H_4 \cdot H_2O$)			CH_3OH yield in 12 h (μmol g^{-1})	327.13	181
$NiSe_2$/g-C_3N_4			C_2H_6 yield (μmol g^{-1} h^{-1})	46.1	190
WSe_2			CH_3OH yield in 10 h (mmol g^{-1} h^{-1})	1.07	180
$NiSe_2$–WSe_2			CH_3OH yield in 10 h (mmol g^{-1} h^{-1})	3.80	180
$Zn_{0.5}Cd_{0.5}S$–$MoTe_2$			CO yield in 3 h (μmol g^{-1})	7.66	183
WTe_2	Photothermal catalytic	300 W, Xe light	C_2H_4 yield in 5 h (μmol g^{-1})	122.9	187

up to 79.6%.[184] In addition, in the study of Cu-embedded on Mo-based TMDs, Cu embedded on $MoTe_2$ provides excellent adsorption energy, demonstrating a lower limiting potential compared to Cu–MoS_2 and Cu–$MoSe_2$.[185]

3.3.6 Tungsten ditelluride (WTe_2). WTe_2 is a TMD with moderate band gap and ultra-high charge mobility, making it suitable for catalysis applications.[186] The catalytic performance of WTe_2 is superior to other W-based TMDs such as WSe_2 and WS_2.[187] WTe_2 can significantly lower the energy barrier and facilitate charge carrier transfer induced by light, hence improving the activity for CO_2 conversion.[187] A comparison of the performance of WTe_2 with other 2D TMDs can be seen in Table 2.

3.3.7 Nickel diselenide ($NiSe_2$). $NiSe_2$, a prominent member of the 2D TMD family, has garnered significant attention for its potential in clean energy applications, particularly in the catalytic reduction of CO_2. The unique structural and electronic properties of $NiSe_2$ facilitate efficient light absorption and charge separation, which are critical for effective photocatalysis. A study has demonstrated that $NiSe_2$ can serve as an effective electrocatalyst, selectively converting CO_2 into valuable carbon-rich products such as C_2H_5OH and acetic acid with a high faradaic efficiency at low applied potentials.[191] This selectivity is attributed to the optimal adsorption energy of the CO intermediates on the $NiSe_2$ surface, promoting C–C bond formation without causing surface passivation. Integrating $NiSe_2$ with other materials has also been considered to further explore its catalytic performance. For instance, the construction of $NiSe_2$/g-C_3N_4 heterojunctions has been shown to promote C–C coupling, leading to the photocatalytic reduction of CO_2 to ethane with high selectivity.[190] In this configuration, $NiSe_2$ serves as a co-catalyst, improving the charge separation and providing active sites for CO_2 adsorption and activation. The synergistic interaction between $NiSe_2$ and g-C_3N_4 results in enhanced visible light absorption and efficient charge transfer, thereby boosting the overall photocatalytic efficiency. Moreover, the combination of $NiSe_2$ with other 2D TMDs, such as WSe_2, has been explored to further improve photocatalytic CO_2 conversion, where the $NiSe_2WSe_2$ composite exhibits a broadened light absorption range and increased specific surface area, leading to a higher yield of CH_3OH during photocatalytic CO_2 reduction.[180] This enhancement is attributed to the improved separation and transfer of photogenerated charge carriers facilitated by the heterojunction, as well as the abundant active sites provided by the composite structure. These findings underscore the potential of $NiSe_2$-based materials in advancing solar energy applications through efficient CO_2 photoreduction processes. Furthermore, a study showed that an octahedral $NiSe_2$ structure supported on $NiTiO_3$ NFs exhibits an exceptional CO_2 photoreduction and higher activity compared to the pristine $NiTiO_3$ by generating more oxygen vacancies and reducing the free energy barrier for COOH* formation.[192]

4 Conclusion and outlook

The device architectures of single and/or tandem cells should be further developed to optimize their PV performances and stability. The attempted integration of 2D TMDs into large-area solar panels may boost the optimism for their utilization in real PV applications.[93] Therefore, further investigation to bring the use of 2D TMDs to the next level should be carried out carefully. Here, all the achieved high performances of 2D TMD-based PV should be also coupled with reliable and safe packaging technology, and then subjected to accelerated life testing under sequential and combined-environmental stress factors such as humidity, temperature, thermal cycles, and mechanical loads. The large-area, uniform, and high-quality growth of 2D TMD layers should be pursued, especially with the development of roll-to-roll deposition.[105] Besides scaling up the growth of 2D TMDs, research efforts should be also deployed to PV device fabrication to large areas with low-cost and robust manufacturing to accelerate their market penetration.

2D TMDs have emerged as versatile candidates in PEC cells, functioning as photoelectrodes, photocatalysts, and co-catalysts. Their tuneable band gap, strong-light matter interactions, and layered architectures enable broad solar absorption and abundant catalytic sites. However, their performance is limited by their inert basal plane, low intrinsic conductivity, and stability issues under reaction conditions. Thus, to overcome these issues, a wide range of engineering methods has been employed. As photoelectrodes, 2D TMDs utilize thin film configurations that provide efficient solar absorption through their tuneable band gap. However, this thin film form still has

a limitation, where weak vdW interactions and large interlayer spacings make thin films vulnerable to electrolyte intercalation and degradation. Thus, to address this issue, engineering several heterostructures with TiO_2, GaN, and ZnO is expected to enhance the charge separation or even protect against photocorrosion. Also, heteroatom doping can be employed to reduce the overpotential and improve the carrier transport. A lower potential leads to easier H_2 evolution. As photocatalysts, 2D TMDs provide high surface-to-volume ratios and tuneable phases. Phase engineering is an effective strategy widely employed to produce 2D TMDs with distinct electronic properties. Specifically, the 1T phase and its distorted variants generally exhibit metallic characteristics, in contrast to the semiconducting 2H and 3R phases. This metallic behaviour allows the 1T and distorted 1T phases to extend the carrier lifetimes by serving as efficient electron transport pathways. Hence, when metallic-like properties are desired, the 1T phase is particularly advantageous. Nevertheless, the 2H phase remains the most thermodynamically stable, making the complete transformation of 2H into the metastable 1T phase a major challenge in synthesizing 2D TMDs for commercial applications. The coexistence of mixed phases (1T/2H) is almost inevitable, and the relative phase ratio significantly influences the device performance. Moreover, the constituent atoms within the 2D TMD layers also play a decisive role in determining their catalytic performance. For instance, with the same transition metal, diselenides typically exhibit superior HER activity compared to disulfides. Consequently, transition metal diselenides are generally preferred for H_2 production applications due to their higher catalytic efficiency. Additionally, atomic defects such as doping and vacancies impart distinct functionalities. The impact of these modifications varies depending on the dopant species and the nature of the vacancy. Compared to complete phase transformation into a single metastable phase, defect engineering provides a more practical and controllable approach for enhancing the properties of 2D TMDs. A wide range of structural modifications has been investigated to improve the performance of 2D TMD-based PEC cells for H_2 generation. Therefore, the summary of previous research presented in this review is expected to provide useful guidelines for future studies in selecting appropriate modification strategies or tandem configurations of 2D TMDs for PEC-driven hydrogen production.

2D TMDs show strong potential for CO_2 photoreduction because of their tuneable bandgaps, broad solar absorption, and catalytic active sites. By converting CO_2 into-value added fuels such as CO, CH_4, CH_3OH, and even C_2 products, these materials not only address GHG emissions, but also provide pathways toward sustainable energy production. Among them, MoS_2 is the most widely studied but limited by its low conductivity and stability. These issues can be minimized by combining it with rGO, SnS_2, or ZnO/In_2O_3 to enhance CO and CH_4 production. Besides, $MoSe_2$ can enhance the charge separation in the heterostructure, achieving higher CO and CH_4 production. Among the W-based diselenides, WS_2 benefits from its phase junctions (1T/2H) and single-atom doping (Cu or Co), while WSe_2 shows improved CO and CH_3OH yields when decorated with Ag nanoparticles. Tellurides such as $MoTe_2$ and WTe_2 are still less explored but exhibit promising CH_4 and C_2H_4 selectivity when embedded with metals or used in composites, although their stability is quite weak. Also, $NiSe_2$ is notable for promoting C–C coupling, enabling C_2 product formation through heterojunctions.

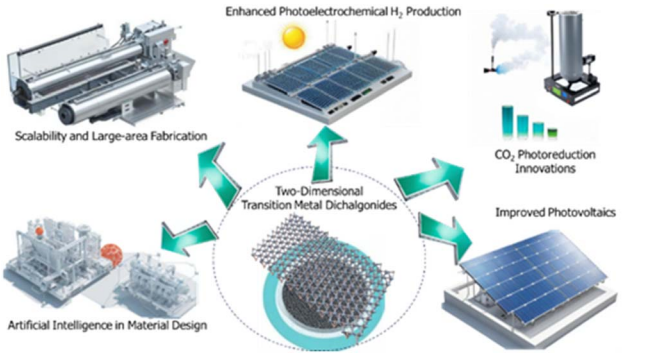

Fig. 13 Outlook on 2D transition metal dichalcogenides (TMDs) for solar energy applications. The central 2D TMD-based nanostructure highlights its potential in scalable fabrication, photovoltaics, photocatalysis, energy storage, hydrogen generation, and solar panels.

Based on these facts, by continuing exploring the unique properties of 2D TMD materials, the future of solar to H_2 conversion can be implemented massively as a manifestation of a sustainable world. Fig. 13 illustrates the broad potential of 2D TMDs in solar energy applications, from large-area fabrication and PV to photocatalysis, energy storage, and H_2 production. 2D TMDs have attracted increasing attention not only in academia but also in industry. Although 2D TMDs exhibit outstanding optoelectronics and catalytic capabilities, their commercial deployment in PVs and photocatalysis has not yet been realized. Developing commercial products for PV applications requires the consideration of several key aspects, including the efficiency of high-power conversion, high stability, low cost, and short recovery period for energy.[193] Several approaches have been developed to reach the commercial feasibility of PV. For instance, WSe_2 PV devices have been explored to achieve a PCE of 5.44% under one-sun AM 1.5G illumination. These PV devices highlighted a number of vdW materials to develop very thin and high-efficiency PV devices.[83] In addition, 2D TMD solar cells (MoS_2, $MoSe_2$, WS_2, and WSe_2) with various thicknesses and indoor lighting conditions have also been explored to be superior to existing indoor PV with PCE reaching 27.6% under low-light AM 1.5G lighting, indicating their potential for commercial indoor PV technologies in the future.[28] In the application of photocatalytic HER, 2D TMDs are also interesting because of their high catalytic performance. Modifying 2D TMDs in a heterojunction structure can regulate their optoelectronic performance better than single layers. The calculated result of the limiting reaction barrier for the $WSe_2/MoSe_2$ heterojunction was 1.13 eV, which is much lower than that of MoS_2 (1.92 eV), indicating its potential for photocatalytic overall water splitting.[194] Although the results are still preliminary, they represent a promising direction for further experimental studies and commercial applications.

Author contributions

K. R. W.: writing – original draft, methodology, editing; L. J. D.: writing – original draft, methodology, writing – review; A. T.: writing – original draft, methodology; I. J. B.: methodology, writing – review; H. J.: supervision, writing – review; A. A.: conceptualization, methodology, writing – review; F. A. A. N.: methodology, writing – review; M. D. B.: conceptualization, methodology, writing – review; A. W.: conceptualization, methodology, funding acquisition, project administration, resources, supervision, writing – review. All authors have given approval to the final version of the manuscript.

Conflicts of interest

There are no conflicts to declare.

Data availability

The data presented in this study are available from the corresponding author on request.

Acknowledgements

A. W. would like to acknowledge the Research, Community Service, and Innovation (P2MI) 2024 scheme from the Faculty of Mechanical and Aerospace Engineering, Institut Teknologi Bandung.

References

1 National Aeronautics and Space Administration, *The Balance of Power in the Earth-Sun System*, 2007.
2 P. K. Nayak, S. Mahesh, H. J. Snaith and D. Cahen, *Nat. Rev. Mater.*, 2019, **4**, 269–285.
3 P. Zhou, I. A. Navid, Y. Ma, Y. Xiao, P. Wang, Z. Ye, B. Zhou, K. Sun and Z. Mi, *Nature*, 2023, **613**, 66–70.
4 A. Azoulay, A. Garcia Baldovi, J. Albero, N. Azaria, J. Tzadikov, A. Tashakory, N. Karjule, S. Hayun, H. García and M. Shalom, *ACS Appl. Energy Mater.*, 2022, **6**, 439–446.
5 P. Ganguly, M. Harb, Z. Cao, L. Cavallo, A. Breen, S. Dervin, D. D. Dionysiou and S. C. Pillai, *ACS Energy Lett.*, 2019, **4**, 1687–1709.
6 M. B. Ananda, M. A. Marsudi, I. J. Budiarso, A. H. Aimon, F. Iskandar, C. Vyas, G. Cooper, P. J. D. S. Bartolo and A. Wibowo, *ChemPhysMater*, 2025, **4**(3), 251–273.
7 P. Jain, R. S. Rajput, S. Kumar, A. Sharma, A. Jain, B. J. Bora, P. Sharma, R. Kumar, M. Shahid, A. A. Rajhi, M. Alsubih, M. A. Shah and A. Bhowmik, *ACS Omega*, 2023, **9**, 12403–12425.
8 Z. Zhou, J. Lv, C. Tan, L. Yang and Z. Wang, *Adv. Funct. Mater.*, 2024, **34**, 2316175.
9 Z. Chen, L. Gui, H. Wang, X. Lu, C. Wu, X. Yang, Y. Li, L. Zhao and S. Wang, *Sep. Purif. Technol.*, 2025, **362**, 131797.
10 M. Nemiwal, T. C. Zhang and D. Kumar, *Int. J. Hydrogen Energy*, 2021, **46**, 21401–21418.
11 S. Mehta, R. Thakur, S. Rani, B. M. Nagaraja, S. Mehla and I. Kainthla, *Int. J. Hydrogen Energy*, 2024, **82**, 1061–1080.
12 C. Hu, Y. K. Jhao, Y. T. Chang, L. H. Kao, K. S. Chuang, J. H. Huang and A. Wibowo, *J. Alloys Compd.*, 2025, **1032**, 181104.
13 T. K. Junita, N. Syakir, F. Faizal and N. Fitrilawati, *ACS Omega*, 2024, **9**, 20658–20669.
14 D. M. Khaidar, W. N. R. W. Isahak, Z. A. C. Ramli and K. N. Ahmad, *Int. J. Hydrogen Energy*, 2024, **68**, 35–50.
15 Q. Xu, Z. Xia, J. Zhang, Z. Wei, Q. Guo, H. Jin, H. Tang, S. Li, X. Pan, Z. Su and S. Wang, *Carbon Energy*, 2023, **5**, e205.
16 D. Monga, S. Sharma, N. P. Shetti, S. Basu, K. R. Reddy and T. M. Aminabhavi, *Mater. Today Chem.*, 2021, **19**, 100399.
17 L. Mennel, V. Smejkal, L. Linhart, J. Burgdörfer, F. Libisch and T. Mueller, *Nano Lett.*, 2020, **20**, 4242–4248.
18 D. Jiang, Z. Liu, Z. Xiao, Z. Qian, Y. Sun, Z. Zeng and R. Wang, *J. Mater. Chem. A*, 2022, **10**, 89–121.
19 H. Khan, H. Charles and C. S. Lee, *J. CO_2 Util.*, 2022, **61**, 102058.
20 Q. Zhang, X. Xiao, R. Zhao, D. Lv, G. Xu, Z. Lu, L. Sun, S. Lin, X. Gao, J. Zhou, C. Jin, F. Ding and L. Jiao, *Angew. Chem., Int. Ed.*, 2015, **54**, 8957–8960.
21 H. Tributsch, *Ber. Bunsenges. Phys. Chem.*, 1977, **81**, 361–369.
22 A. Sobczynskv, A. Yildiz, A. J. Bard, A. Campion, A. Fox, T. Mallouk, S. E. Webber and J. M. White, *J. Phys. Chem.*, 1988, **92**, 2311–2315.
23 X. Zong, H. Yan, G. Wu, G. Ma, F. Wen, L. Wang and C. Li, *J. Am. Chem. Soc.*, 2008, **130**, 7176–7177.
24 K. F. Mak, C. Lee, J. Hone, J. Shan and T. F. Heinz, *Phys. Rev. Lett.*, 2010, **105**, 136805.
25 X. Hong, J. Kim, S. F. Shi, Y. Zhang, C. Jin, Y. Sun, S. Tongay, J. Wu, Y. Zhang and F. Wang, *Nat. Nanotechnol.*, 2014, **9**, 682–686.
26 A. Ali and W. C. Oh, *Sci. Rep.*, 2017, **7**, 1–11.
27 A. Abnavi, R. Ahmadi, H. Ghanbari, M. Fawzy, A. Hasani, T. De Silva, A. M. Askar, M. R. Mohammadzadeh, F. Kabir, M. Whitwick, M. Beaudoin, S. K. O'Leary and M. M. Adachi, *Adv. Funct. Mater.*, 2023, **33**, 2210619.
28 F. U. Nitta, K. Nassiri Nazif and E. Pop, *Device*, 2025, **3**, 100723.
29 R. Sukanya, D. C. da Silva Alves and C. B. Breslin, *J. Electrochem. Soc.*, 2022, **169**, 064504.
30 F. Bozheyev, *Curr. Opin. Electrochem.*, 2022, **34**, 100995.
31 S. Manzeli, D. Ovchinnikov, D. Pasquier, O. V. Yazyev and A. Kis, *Nat. Rev. Mater.*, 2017, **2**, 17033.
32 Q. Zhang, A. T. S. Wee, Q. Liang, X. Zhao and M. Liu, *ACS Nano*, 2021, **15**, 2165–2181.
33 Z. Li, Y. Song and S. Tang, *J. Phys.:Condens. Matter*, 2020, **32**, 33001.
34 G. H. Han, D. L. Duong, D. H. Keum, S. J. Yun and Y. H. Lee, *Chem. Rev.*, 2018, **118**, 6297–6336.
35 X. Qian, J. Liu, L. Fu and J. Li, *Science*, 2014, **346**, 1344–1347.
36 H. Li, Y. Shi, M. H. Chiu and L. J. Li, *Nano Energy*, 2015, **18**, 293–305.

37 C. Gong, Y. Zhang, W. Chen, J. Chu, T. Lei, J. Pu, L. Dai, C. Wu, Y. Cheng, T. Zhai, L. Li and J. Xiong, *Adv. Sci.*, 2017, **4**, 1700231.
38 T. Tan, X. Jiang, C. Wang, B. Yao and H. Zhang, *Adv. Sci.*, 2020, **7**, 2000058.
39 S. Omnia and E. M. Amine, *Energies*, 2021, **14**, 35–51.
40 W. Choi, N. Choudhary, G. H. Han, J. Park, D. Akinwande and Y. H. Lee, *Mater. Today*, 2017, **20**, 116–130.
41 W. Zhao, J. Pan, Y. Fang, X. Che, D. Wang and K. Bu, *Chem.–Eur. J.*, 2018, **24**, 15942–15954.
42 S. Padmajan Sasikala, Y. Singh, L. Bing, T. Yun, S. H. Koo, Y. Jung and S. O. Kim, *Nat. Commun.*, 2020, **11**, 5032.
43 S. Tang, C. Zhang, D. Wong, Z. Pedramrazi, H. Tsai, C. Jia, B. Moritz, M. Claassen, H. Ryu, S. Kahn, J. Jiang, H. Yan, M. Hashimoto, D. Lu, R. G. Moore, C. Hwang, C. Hwang, Z. Hussain, Y. Chen, M. M. Ugeda, Z. Liu and X. Xie, *Nat. Phys.*, 2017, **13**, 683–688.
44 Z. Zeng, Z. Yin, X. Huang, H. Li, Q. He, G. Lu, F. Boey and H. Zhang, *Angew. Chem., Int. Ed.*, 2011, **50**, 11093–11097.
45 B. L. Li, J. Wang, H. L. Zou, S. Garaj, C. T. Lim, J. Xie, N. B. Li and D. T. Leong, *Adv. Funct. Mater.*, 2016, **26**, 7034–7056.
46 J. Zheng, H. Zhang, S. Dong, Y. Liu, C. Tai Nai, H. Suk Shin, H. Young Jeong, B. Liu and K. Ping Loh, *Nat. Commun.*, 2014, **5**, 1–7.
47 T. Chowdhury, E. C. Sadler and T. J. Kempa, *Chem. Rev.*, 2020, **120**, 12563–12591.
48 Y. Zhao, K. Xu, F. Pan, C. Zhou, F. Zhou and Y. Chai, *Adv. Funct. Mater.*, 2017, **27**, 1603484.
49 V. Kochat, A. Apte, J. A. Hachtel, H. Kumazoe, A. Krishnamoorthy, S. Susarla, J. C. Idrobo, F. Shimojo, P. Vashishta, R. Kalia, A. Nakano, C. S. Tiwary and P. M. Ajayan, *Adv. Mater.*, 2017, **29**, 1–8.
50 K. Chang, X. Hai, H. Pang, H. Zhang, L. Shi, G. Liu and H. Liu, *Adv. Mater.*, 2016, **28**, 10033–10041.
51 R. J. Toh, Z. Sofer, J. Luxa, D. Sedmidubsky and M. Pumera, *Chem. Commun.*, 2017, **53**, 3054–3057.
52 I. Shahbaz, M. Tahir, L. Li and Y. Song, *Mater. Today*, 2024, **77**, 142–184.
53 A. Splendiani, L. Sun, Y. Zhang, T. Li, J. Kim, C. Y. Chim, G. Galli and F. Wang, *Nano Lett.*, 2010, **10**, 1271–1275.
54 C. Zhang, C. Gong, Y. Nie, K. A. Min, C. Liang, Y. J. Oh, H. Zhang, W. Wang, S. Hong, L. Colombo, R. M. Wallace and K. Cho, *2D Mater.*, 2017, **4**, 015026.
55 J. S. Ponraj, Z. Q. Xu, S. C. Dhanabalan, H. Mu, Y. Wang, J. Yuan, P. Li, S. Thakur, M. Ashrafi, K. McCoubrey, Y. Zhang, S. Li, H. Zhang and Q. Bao, *Nanotechnology*, 2016, **27**, 1–33.
56 M. Onga, Y. Zhang, T. Ideue and Y. Iwasa, *Nat. Mater.*, 2017, **16**, 1193–1197.
57 X. Zhou, X. Hu, J. Yu, S. Liu, Z. Shu, Q. Zhang, H. Li, Y. Ma, H. Xu and T. Zhai, *Adv. Funct. Mater.*, 2018, **28**, 1706587.
58 L. Pi, L. Li, K. Liu, Q. Zhang, H. Li and T. Zhai, *Adv. Funct. Mater.*, 2019, **29**, 1904932.
59 Y. Liu, Z. Yang, Z. Jiang, Q. Qian, S. Zhou, W. Cao, H. Liu, K. Qian, L. Han and R. Cao, *ACS Appl. Energy Mater.*, 2024, **7**, 9986–9995.
60 H. Li, C. Tsai, A. L. Koh, L. Cai, A. W. Contryman, A. H. Fragapane, J. Zhao, H. S. Han, H. C. Manoharan, F. Abild-Pedersen, J. K. Nørskov and X. Zheng, *Nat. Mater.*, 2016, **15**, 48–53.
61 S. Tanwar, A. Arya, A. Gaur and A. L. Sharma, *J. Phys.:Condens. Matter*, 2021, **33**, 303002.
62 W. Zhou, X. Zou, S. Najmaei, Z. Liu, Y. Shi, J. Kong, J. Lou, P. M. Ajayan, B. I. Yakobson and J. C. Idrobo, *Nano Lett.*, 2013, **13**, 2615–2622.
63 Q. Fu, J. Han, X. Wang, P. Xu, T. Yao, J. Zhong, W. Zhong, S. Liu, T. Gao, Z. Zhang, L. Xu and B. Song, *Adv. Mater.*, 2021, **33**, 1907818.
64 D. Nayak and R. Thangavel, *J. Mater. Sci.*, 2022, **57**, 4283–4299.
65 Z. Yu, Z. Ong, S. Li, J. Xu, G. Zhang, Y. Zhang, Y. Shi and X. Wang, *Adv. Funct. Mater.*, 2017, **27**, 1604093.
66 F. Hu, L. Tao, H. Ye, X. Li and X. Chen, *J. Mater. Chem. C*, 2019, **7**, 7104–7113.
67 M. Ahmadi, O. Zabihi, S. Jeon, M. Yoonessi, A. Dasari, S. Ramakrishna and M. Naebe, *J. Mater. Chem. A*, 2019, **8**, 845–883.
68 F. Wang, Z. Wang, K. Xu, F. Wang, Q. Wang, Y. Huang, L. Yin and J. He, *Nano Lett.*, 2015, **15**, 7558–7566.
69 L. Li, H. Shi, H. Yu, X. Tan, Y. Wang, S. Ge, A. Wang, K. Cui, L. Zhang and J. Yu, *Appl. Catal., B*, 2021, **292**, 120184.
70 Z. Hu, Z. Wu, C. Han, J. He, Z. Ni and W. Chen, *Chem. Soc. Rev.*, 2018, **47**, 3100–3128.
71 Y. Gong, J. Lin, X. Wang, G. Shi, S. Lei, Z. Lin, X. Zou, G. Ye, R. Vajtai, B. I. Yakobson, H. Terrones, M. Terrones, B. K. Tay, J. Lou, S. T. Pantelides, Z. Liu, W. Zhou and P. M. Ajayan, *Nat. Mater.*, 2014, **13**, 1135–1142.
72 M. Bernardi, M. Palummo and J. C. Grossman, *Nano Lett.*, 2013, **13**, 3664–3670.
73 K. Wu, H. Ma, Y. Gao, W. Hu and J. Yang, *J. Mater. Chem. A*, 2019, **7**, 7430–7436.
74 C. M. Went, J. Wong, P. R. Jahelka, M. Kelzenberg, S. Biswas, M. S. Hunt, A. Carbone and H. A. Atwater, *Sci. Adv.*, 2019, **5**, eaax6061.
75 A. C. Dias, H. Bragança, J. P. A. De Mendonça and J. L. F. Da Silva, *ACS Appl. Energy Mater.*, 2021, **4**, 3265–3278.
76 D. Singh and R. Ahuja, *ACS Appl. Energy Mater.*, 2022, **5**, 2300–2307.
77 S. Aftab, M. A. Shehzad, H. M. Salman Ajmal, F. Kabir, M. Z. Iqbal and A. A. Al-Kahtani, *ACS Nano*, 2023, **17**, 17884–17896.
78 K. Nassiri Nazif, F. U. Nitta, A. Daus, K. C. Saraswat and E. Pop, *Commun. Phys.*, 2023, **6**, 367.
79 M. M. Furchi, F. Höller, L. Dobusch, D. K. Polyushkin, S. Schuler and T. Mueller, *npj 2D Mater. Appl.*, 2018, **2**, 3.
80 A. J. Cho, M. K. Song, D. W. Kang and J. Y. Kwon, *ACS Appl. Mater. Interfaces*, 2018, **10**, 35972–35977.
81 S. Yang, J. Cha, J. C. Kim, D. Lee, W. Huh, Y. Kim, S. W. Lee, H. G. Park, H. Y. Jeong, S. Hong, G. H. Lee and C. H. Lee, *Nano Lett.*, 2020, **20**, 2443–2451.
82 K. N. Nazif, A. Daus, J. Hong, N. Lee, S. Vaziri, A. Kumar, F. Nitta, M. E. Chen, S. Kananian, R. Islam, K. H. Kim,

J. H. Park, A. S. Y. Poon, M. L. Brongersma, E. Pop and K. C. Saraswat, *Nat. Commun.*, 2021, **12**, 7034.
83 K. H. Kim, M. Andreev, S. Choi, J. Shim, H. Ahn, J. Lynch, T. Lee, J. Lee, K. N. Nazif, A. Kumar, P. Kumar, H. Choo, D. Jariwala, K. C. Saraswat and J. H. Park, *ACS Nano*, 2022, **16**, 8827–8836.
84 M. L. Tsai, M. Y. Li, J. R. D. Retamal, K. T. Lam, Y. C. Lin, K. Suenaga, L. J. Chen, G. Liang, L. J. Li and J. H. He, *Adv. Mater.*, 2017, **29**, 1701168.
85 M. Gholipoor, N. Solhtalab and M. H. Mohammadi, *Sci. Rep.*, 2022, **12**, 20455.
86 H. Yang, Y. Hao, J. Ren, Y. Wu, Q. Sun, C. Zhang, Y. Cui and Y. Hao, *J. Mater. Chem. C*, 2023, **11**, 8470–8479.
87 P. Huang, Z. Wang, Y. Liu, K. Zhang, L. Yuan, Y. Zhou, B. Song and Y. Li, *ACS Appl. Mater. Interfaces*, 2017, **9**, 25323–25331.
88 Z. Lei, J. Zhan, L. Tang, Y. Zhang and Y. Wang, *Adv. Energy Mater.*, 2018, **8**, 1703482.
89 S. X. Leong, C. C. Mayorga-Martinez, X. Chia, J. Luxa, Z. Sofer and M. Pumera, *ACS Appl. Mater. Interfaces*, 2017, **9**, 26350–26356.
90 M. Liang, A. Ali, A. Belaidi, M. I. Hossain, O. Ronan, C. Downing, N. Tabet, S. Sanvito, F. EI-Mellouhi and V. Nicolosi, *npj 2D Mater. Appl.*, 2020, **4**, 40.
91 A. Agresti, S. Pescetelli, A. L. Palma, B. Martín-García, L. Najafi, S. Bellani, I. Moreels, M. Prato, F. Bonaccorso and A. Di Carlo, *ACS Energy Lett.*, 2019, **4**, 1862–1871.
92 S. Pescetelli, A. Agresti, S. Razza, H. Pazniak, L. Najafi, F. Bonaccorso and A. Di Carlo, *Nano Energy*, 2022, **95**, 107019.
93 S. Pescetelli, A. Agresti, G. Viskadouros, S. Razza, K. Rogdakis, I. Kalogerakis, E. Spiliarotis, E. Leonardi, P. Mariani, L. Sorbello, M. Pierro, C. Cornaro, S. Bellani, L. Najafi, B. Martín-García, A. E. Del Rio Castillo, R. Oropesa-Nuñez, M. Prato, S. Maranghi, M. L. Parisi, A. Sinicropi, R. Basosi, F. Bonaccorso, E. Kymakis and A. Di Carlo, *Nat. Energy*, 2022, **7**, 597–607.
94 N. Alias, A. Ali Umar, N. A. A. Malek, K. Liu, X. Li, N. A. Abdullah, M. M. Rosli, M. Y. A. Rahman, Z. Shi, X. Zhang, H. Zhang, F. Liu, J. Wang and Y. Zhan, *ACS Appl. Mater. Interfaces*, 2021, **13**, 3051–3061.
95 B. Kim, M. Kim, H. Kim, S. Jeong, J. Yang and M. S. Jeong, *ACS Appl. Mater. Interfaces*, 2022, **14**, 35726–35733.
96 Z. Dou, X. Cheng, Z. Qin, K. Wang, W. Xia, Y. Qu, H. Lian, F. Yan and Q. Dong, *Sol. RRL*, 2024, **8**, 2300693.
97 H. Li, B. Yu and H. Yu, *Adv. Funct. Mater.*, 2024, **34**, 2402128.
98 L. T. L. Lee, J. He, B. Wang, Y. Ma, K. Y. Wong, Q. Li, X. Xiao and T. Chen, *Sci. Rep.*, 2014, **4**, 4063.
99 Y. Areerob, W. C. Oh, C. Hamontree, T. Nachaithong, S. Nijpanich and K. Pattarith, *Sci. Rep.*, 2023, **13**, 7762.
100 D. Vikraman, A. A. Arbab, S. Hussain, N. K. Shrestha, S. H. Jeong, J. Jung, S. A. Patil and H. S. Kim, *ACS Sustain. Chem. Eng.*, 2019, **7**, 13195–13205.
101 S. Hussain, S. A. Patil, D. Vikraman, I. Rabani, A. A. Arbab, S. H. Jeong, H. S. Kim, H. Choi and J. Jung, *Appl. Surf. Sci.*, 2020, **504**, 144401.
102 D. Vikraman, S. Hussain, S. A. Patil, L. Truong, A. A. Arbab, S. H. Jeong, S. H. Chun, J. Jung and H. S. Kim, *ACS Appl. Mater. Interfaces*, 2021, **13**, 5061–5072.
103 M. C. Sorkun, S. Astruc, J. M. V. A. Koelman and S. Er, *npj Comput. Mater.*, 2020, **6**, 106.
104 B. Sa, R. Hu, Z. Zheng, R. Xiong, Y. Zhang, C. Wen, J. Zhou and Z. Sun, *Chem. Mater.*, 2022, **34**, 6687–6701.
105 R. A. Wells, H. Johnson, C. R. Lhermitte, S. Kinge and K. Sivula, *ACS Appl. Nano Mater.*, 2019, **2**, 7705–7712.
106 U. K. Zore, S. G. Yedire, N. Pandi, S. Manickam and S. H. Sonawane, *Ultrason. Sonochem.*, 2021, **73**, 105536.
107 J. Ke, F. He, H. Wu, S. Lyu, J. Liu, B. Yang, Z. Li, Q. Zhang, J. Chen, L. Lei, Y. Hou and K. Ostrikov, *Nano-Micro Lett.*, 2020, **13**, 24.
108 M. Rahman, K. Davey and S. Z. Qiao, *Adv. Funct. Mater.*, 2017, **27**, 1606129.
109 D. M. Andoshe, J. M. Jeon, S. Y. Kim and H. W. Jang, *Electron. Mater. Lett.*, 2015, **11**, 323–335.
110 X. Lu, Y. Lu, C. Wang and Y. Cao, *Rare Met.*, 2022, **41**, 1142–1159.
111 X. Yu, M. S. Prevot, N. Guijarro and K. Sivula, *Nat. Commun.*, 2015, **6**, 7596.
112 A. R. Fareza, F. A. A. Nugroho and V. Fauzia, *ACS Appl. Nano Mater.*, 2022, **5**, 16051–16060.
113 S. Sambyal, A. Sudhaik, S. Sonu, P. Raizada, V. Chaudhary, V. H. Nguyen, A. A. P. Khan, C. M. Hussain and P. Singh, *Coord. Chem. Rev.*, 2025, **535**, 216653.
114 I. H. Kwak, I. S. Kwon, J. H. Lee, Y. R. Lim and J. Park, *J. Mater. Chem. C*, 2021, **9**, 101–109.
115 R. Sharma, M. Khanuja, S. N. Sharma and O. P. Sinha, *Int. J. Hydrogen Energy*, 2017, **42**, 20638–20648.
116 L. Lin, P. Sherrell, Y. Liu, W. Lei, S. Zhang, H. Zhang, G. G. Wallace and J. Chen, *Adv. Energy Mater.*, 2020, **10**, 1903870.
117 A. Hardiansyah, W. J. Budiman, N. Yudasari, Isnaeni, T. Kida and A. Wibowo, *ACS Omega*, 2021, **6**, 32166–32177.
118 I. J. Budiarso, S. Fujita, S. Saito, H. Judawisastra, K. Takeyasu and A. Wibowo, *React. Chem. Eng.*, 2024, **9**, 2718–2727.
119 I. J. Budiarso, V. A. Dabur, R. Rachmantyo, H. Judawisastra, C. Hu and A. Wibowo, *Mater. Adv.*, 2024, **5**, 2668–2688.
120 A. Chawla, A. Sudhaik, Sonu, R. Kumar, P. Raizada, T. Ahamad, A. A. P. Khan, Q. Van Le, V. H. Nguyen, S. Thakur and P. Singh, *Coord. Chem. Rev.*, 2025, **529**, 216443.
121 R. Yang, Y. Fan, Y. Zhang, L. Mei, R. Zhu, J. Qin, J. Hu, Z. Chen, Y. Hau Ng, D. Voiry, S. Li, Q. Lu, Q. Wang, J. C. Yu and Z. Zeng, *Angew. Chem., Int. Ed.*, 2023, **62**, e202218016.
122 Y. Zhao, S. Zhang, R. Shi, G. I. N. Waterhouse, J. Tang and T. Zhang, *Mater. Today*, 2020, **34**, 78–91.
123 E. V Sukhanova, N. Sagatov and A. S. Oreshonkov, *Int. J. Hydrogen Energy*, 2022, **48**, 14226–14237.
124 Z. Masoumi, M. Tayebi, M. Kolaei and B. Lee, *Appl. Catal., B*, 2022, **313**, 121447.

125 D. Mouloua, T. Vicart, N. S. Rajput, B. Asbani, M. El Marssi, M. A. El Khakani and M. Jouiad, *J. Colloid Interface Sci.*, 2025, **687**, 851–859.
126 L. Lin, P. Sherrell, Y. Liu, W. Lei, S. Zhang, H. Zhang, G. G. Wallace and J. Chen, *Adv. Energy Mater.*, 2020, **10**, 1903870.
127 H. H. Huang, X. Fan, D. J. Singh and W. T. Zheng, *Nanoscale*, 2020, **12**, 1247–1268.
128 M. H. Jameel, M. S. bin Roslan, M. Z. H. Bin Mayzan, I. A. Shaaban, S. Z. H. Rizvi, M. A. Bin Agam, S. Saleem and M. A. Assiri, *J. Inorg. Organomet. Polym. Mater.*, 2024, **34**, 322–335.
129 Z. Gholamvand, D. McAteer, C. Backes, N. McEvoy, A. Harvey, N. C. Berner, D. Hanlon, C. Bradley, I. Godwin, A. Rovetta, M. E. G. Lyons and S. Duesberg, *Nanoscale*, 2016, **6**, 5737–5749.
130 E. Son, S. Lee, J. Seo, U. Kim, S. H. Kim, J. M. Baik, Y. K. Han and H. Park, *ACS Nano*, 2023, **17**, 10817–10826.
131 T. X. Huang, B. Dong, S. L. Filbrun, A. A. Okmi, X. Cheng, M. Yang, N. Mansour, S. Lei and N. Fang, *Sci. Adv.*, 2021, **7**, eabj4425.
132 Y. Yan, Z. Zeng, M. Huang and P. Chen, *Mater. Today Adv.*, 2020, **6**, 100059.
133 G. Zhao, K. Rui, S. X. Dou and W. Sun, *Adv. Funct. Mater.*, 2018, **28**, 1803291.
134 X. Ma, X. Wu, H. Wang and Y. Wang, *J. Mater. Chem. A*, 2018, **6**, 2295–2301.
135 Z. Guan, S. Ni and S. Hu, *J. Phys. Chem. C*, 2018, **122**, 6209–6216.
136 X. Xiong, H. Yang, J. Zhang, J. Lin, S. Yang, C. Chen, J. Xi, Z. Kong, L. Song and J. Zeng, *J. Alloys Compd.*, 2023, **933**, 167784.
137 K. Chang, X. Hai and J. Ye, *Adv. Energy Mater.*, 2016, **6**, 1502555.
138 W. Peng, Y. Li, F. Zhang, G. Zhang and X. Fan, *Ind. Eng. Chem. Res.*, 2017, **56**, 4611–4626.
139 R. Tong, K. W. Ng, X. Wang, S. Wang, X. Wang and H. Pan, *J. Mater. Chem. A*, 2020, **8**, 23202–23230.
140 F. R. H. Rayanisaputri, D. Aryanto, L. Bijelić, A. Susarrey-Arce, F. Ruiz-Zepeda, F. A. A. Nugroho and V. Fauzia, *ACS Appl. Nano Mater.*, 2025, **8**, 1479–1489.
141 A. R. Fareza, L. Roza, F. A. A. Nugroho and V. Fauzia, *Surf. Interfaces*, 2023, **37**, 102663.
142 J. Yi, X. She, Y. Song, M. Mao, K. Xia, Y. Xu, Z. Mo, J. Wu, H. Xu and H. Li, *Chem. Eng. J.*, 2018, **335**, 282–289.
143 J. Yu, Y. Wang, Z. Luan, X. Sun, Y. Liang, W. Liu, B. Zhong and X. Fan, *Int. J. Hydrogen Energy*, 2024, **93**, 59–67.
144 K. Roy, S. Maitra, D. Ghosh, P. Kumar and P. Devi, *Chem. Eng. J.*, 2022, **435**, 134963.
145 Q. Jing, H. Zhang, H. Huang, X. Fan, Y. Zhang, X. Hou, Q. Xu, Z. Ni and T. Qiu, *Nanotechnology*, 2019, **30**, 184001.
146 S. A. Ali and T. Ahmad, *Int. J. Hydrogen Energy*, 2023, **48**, 22044–22059.
147 M. Rezaei, A. A. Ensafi and E. Heydari-Bafrooei, *J. Ind. Eng. Chem.*, 2025, **146**, 589–602.
148 J. Wang, H. Shu, P. Liang, N. Wang, D. Cao and X. Chen, *J. Phys. Chem. C*, 2019, **123**, 3861–3867.
149 A. Degg, K. Vosseler, N. Kumar, N. Chaulagain, M. R. P. Pielmeier, T. Nilges and K. Shankar, *Z. Anorg. Allg. Chem.*, 2025, **651**, e202400129.
150 S. A. Ali, S. Majumdar, P. K. Chowdhury, N. Alhokbany and T. Ahmad, *ACS Appl. Energy Mater.*, 2024, **7**, 2881–2895.
151 S. A. Ali, S. Majumdar, P. K. Chowdhury, S. M. Alshehri and T. Ahmad, *ACS Appl. Energy Mater.*, 2024, **7**, 7325–7337.
152 J. H. Li, Y. Zhang, S. Z. Sun, Y. Sen Yang, Y. F. Luo and L. Duan, *Micro Nanostruct.*, 2024, **195**, 207953.
153 J. C. McGlynn, T. Dankwort, L. Kienle, N. A. G. Bandeira, J. P. Fraser, E. K. Gibson, I. Cascallana-Matías, K. Kamarás, M. D. Symes, H. N. Miras and A. Y. Ganin, *Nat. Commun.*, 2019, **10**, 4916.
154 J. Yang, T. Lü, Y. W. Myint, J. Pei, D. Macdonald, J. C. Zheng and Y. Lu, *ACS Nano*, 2015, **9**, 6603–6609.
155 Q. Zhang, X. Bai, X. Hu, J. Fan and E. Liu, *Appl. Surf. Sci.*, 2022, **579**, 152224.
156 Q. Zhang, J. Jia, J. Fan, X. Hu, E. Liu and D. Yang, *Int. J. Hydrogen Energy*, 2020, **45**, 13340–13352.
157 L. Cheng, J. Abraham, K. E. Trenberth, J. Reagan, H. M. Zhang, A. Storto, K. Von Schuckmann, Y. Pan, Y. Zhu, M. E. Mann, J. Zhu, F. Wang, F. Yu, R. Locarnini, J. Fasullo, B. Huang, G. Graham, X. Yin, V. Gouretski, F. Zheng, Y. Li, B. Zhang, L. Wan, X. Chen, D. Wang, L. Feng, X. Song, Y. Liu, F. Reseghetti, S. Simoncelli, G. Chen, R. Zhang, A. Mishonov, Z. Tan, W. Wei, H. Yuan, G. Li, Q. Ren, L. Cao, Y. Lu, J. Du, K. Lyu, A. Sulaiman, M. Mayer, H. Wang, Z. Ma, S. Bao, H. Yan, Z. Liu, C. Yang, X. Liu, Z. Hausfather, T. Szekely and F. Gues, *Adv. Atmos. Sci.*, 2025, **42**, 1092–1109.
158 J. E. Hansen, P. Kharecha, M. Sato, G. Tselioudis, J. Kelly, S. E. Bauer, R. Ruedy, E. Jeong, Q. Jin, E. Rignot, I. Velicogna, M. R. Schoeberl, K. von Schuckmann, J. Amponsem, J. Cao, A. Keskinen, J. Li and A. Pokela, *Environment*, 2025, **67**, 6–44.
159 M. D. Mathew, *Prog. Nucl. Energy*, 2022, **143**, 104080.
160 T. Zhong, Z. Yu, R. Jiang, J. Huang, Y. Hou, J. Chen, Y. Zhang, H. Zhu, B. Wang and L. Ding, *Sol. RRL*, 2021, **5**, 2100223.
161 Y. Wang, J. Zhao, Z. Chen, F. Zhang, W. Guo, H. Lin and F. Qu, *Appl. Catal., B*, 2019, **244**, 76–86.
162 Y. Song, W. Chen, W. Wei and Y. Sun, *Catalysts*, 2020, **10**, 1287.
163 Y. Xie, Y. Zhou, C. Gao, L. Liu, Y. Zhang, Y. Chen and Y. Shao, *Sep. Purif. Technol.*, 2022, **303**, 122288.
164 H. Zhou, Y. Hu, Y. Zhang, W. Jiang and J. Di, *Sep. Purif. Technol.*, 2025, **359**, 130549.
165 H. Li, T. Sun, L. Zhang and Y. Cao, *Appl. Surf. Sci.*, 2021, **566**, 150649.
166 B. Kaur, P. Singh, A. Singh, Q. Van Le, V. Chaudhary, V. H. Nguyen, M. Asad, A. A. P. Khan, H. M. Marwani and P. Raizada, *J. Environ. Chem. Eng.*, 2025, **13**, 116904.
167 A. Azhar, M. A. Basit, W. Mehmood, M. A. Ali, S. Zahid, M. Ahmad, S. J. A. Zaidi and T. J. Park, *Colloids Surf., A*, 2023, **657**, 130581.
168 H. Khan, R. C. Pawar, H. Charles and C. Sunyong Lee, *Appl. Surf. Sci.*, 2023, **636**, 157832.

169 G. S. Selvam, T. Dheivasigamani, A. Prabhu and N. K. Mani, *ACS Omega*, 2022, **7**, 24606–24613.
170 S. Kang, H. Khan, C. Lee, K. Kwon and C. Sunyong Lee, *Chem. Eng. J.*, 2021, **420**, 130496.
171 L. T. Samosir, F. A. A. Nugroho and V. Fauzia, *Electrochim. Acta*, 2024, **496**, 144483.
172 R. A. Geioushy, S. M. El-Sheikh, I. M. Hegazy, A. Shawky, S. El-Sherbiny and A. H. T. Kandil, *Mater. Res. Bull.*, 2019, **118**, 110499.
173 J. Jiang, X. Zou, Z. Mei, S. Cai, Q. An, Y. Fu, H. Wang, T. Liu and H. Guo, *J. Colloid Interface Sci.*, 2022, **611**, 644–653.
174 S. Yin, J. Li, L. Sun, X. Li, D. Shen, X. Song, P. Huo, H. Wang and Y. Yan, *Inorg. Chem.*, 2019, **58**, 15590–15601.
175 L. Zhou, J. Xu, S. Wei, L. Liu, Z. Zhou and X. Liu, *Carbon Capture Sci. Technol.*, 2024, **12**, 100223.
176 L. J. Chen, T. T. Liu, S. M. Liu, S. Cai, X. X. Zou, J. W. Jiang, Z. Y. Mei, G. F. Zhao, X. F. Yang and H. Guo, *Rare Met.*, 2021, **41**, 144–154.
177 A. G. Alhamzani, T. A. Yousef, M. M. Abou-Krisha, K. Y. Kumar, M. K. Prashanth, L. Parashuram, B. Hun Jeon and M. S. Raghu, *Chemosphere*, 2023, **322**, 138235.
178 Y. Zhou, Q. Ye, X. Shi, Q. Zhang, Z. Xie, D. Li and D. Jiang, *Chem. Eng. J.*, 2022, **447**, 137485.
179 P. M. Ismail, S. Ali, F. Raziq, M. Bououdina, H. Abu-Farsakh, P. Xia, X. Wu, H. Xiao, S. Ali and L. Qiao, *Appl. Surf. Sci.*, 2023, **624**, 157073.
180 Z. Luo, Y. Li, F. Guo, K. Zhang, K. Liu, W. Jia, Y. Zhao and Y. Sun, *Energies*, 2020, **13**, 4330.
181 Z. Luo, Y. H. Li, F. B. Guo, L. X. Zhang, B. Hou, J. C. Guo and S. N. Wang, *IOP Conf. Ser. Earth Environ. Sci.*, 2021, **701**, 012043.
182 X. Chen, Y. Wang, J. Lang, L. Wu, C. Yan and Y. Li, *Mater. Lett.*, 2024, **362**, 136139.
183 Z. Yuan, Y. Xiang, X. Jian, H. Zhang, M. Liu, R. Cao and Y. Hu, *Sep. Purif. Technol.*, 2025, **359**, 129836.
184 K. Wang, Z. Hu, P. Yu, A. M. Balu, K. Li and L. Li, *Nano-Micro Lett.*, 2024, **16**, 5.
185 T. Doulassiramane and R. Padmanaban, *Langmuir*, 2024, **41**, 329–339.
186 X. Zhang, Y. Yang, Y. Hu, L. Xiong, T. Wang, P. Li and J. Shen, *J. Energy Chem.*, 2024, **93**, 547–556.
187 X. Zhang, Y. Yang, Y. Hu, Y. Chen, J. Shen and Y. Tu, *ACS Appl. Energy Mater.*, 2024, **7**, 11859–11872.
188 A. Saxena, W. P. R. Liyanage, S. Kapila and M. Nath, *Catal. Sci. Technol.*, 2022, **12**, 4727–4739.
189 J. Jia, Y. Luo, H. Wu, Y. Wang, X. Jia, J. Wan, Y. Dang, G. Liu, H. Xie and Y. Zhang, *J. Colloid Interface Sci.*, 2024, **658**, 966–975.
190 F. Temerov, R. Greco, J. Celis, S. Eslava, W. Wang, T. Yamamoto and W. Cao, *Results Mater.*, 2024, **22**, 100569.
191 R. Ud, D. Biswas, A. Ali, K. Youn and W. Oh, *Ultrason. Sonochem.*, 2018, **42**, 738–746.
192 H. Khan, R. C. Pawar, H. Charles, P. J. Changula and C. S. Lee, *Appl. Surf. Sci.*, 2023, **629**, 157362.
193 L. Meng, J. You and Y. Yang, *Nat. Commun.*, 2018, **9**, 5265.
194 J. Ma, J. Pang, J. Yang, W. Xie, X. Kuang and A. Mao, *J. Mater. Chem. A*, 2025, **13**, 9312–9322.